Modeling the Sources and Chemistry of Polar Tropospheric Halogens (Cl, Br, and I) Using the CAM-Chem Global Chemistry-Climate Model

Rafael P. Fernandez[1,2] , Antía Carmona-Balea[1], Carlos A. Cuevas[1] , Javier A. Barrera[2], Douglas E. Kinnison[3], Jean-Francois Lamarque[3] , Christopher Blaszczak-Boxe[4,5], Kitae Kim[6,7], Wonyong Choi[8], Timothy Hay[9] , Anne-Marlene Blechschmidt[10], Anja Schönhardt[10], John P. Burrows[10] , and Alfonso Saiz-Lopez[1]

[1]Department of Atmospheric Chemistry and Climate, Institute of Physical Chemistry Rocasolano, CSIC, Madrid, Spain, [2]National Research Council (CONICET), FCEN-UNCuyo, UNT-FRM, Mendoza, Argentina, [3]Atmospheric Chemistry, Observations & Modeling Laboratory, National Center for Atmospheric Research, Boulder, CO, USA, [4]Department of Chemistry & Environmental Science, Medgar Evers College-City University of New York, Brooklyn, NY, USA, [5]Chemistry Division, Earth and Environmental Science Division, CUNY Graduate Center, Manhattan, NY, USA, [6]Department of Polar Sciences, University of Science and Technology, Incheon, South Korea, [7]Korea Polar Research Institute (KOPRI), Incheon, South Korea, [8]Division of Environmental Science and Engineering, Pohan University of Science and Technology (POSTECH), Pohan, South Korea, [9]National Institute of Water and Atmospheric Research (NIWA), Lauder, New Zealand, [10]Institute of Environmental Physics, University of Bremen, Bremen, Germany

Abstract Current chemistry climate models do not include polar emissions and chemistry of halogens. This work presents the first implementation of an interactive polar module into the very short-lived (VSL) halogen version of the Community Atmosphere Model with Chemistry (CAM-Chem) model. The polar module includes photochemical release of molecular bromine, chlorine, and interhalogens from the sea-ice surface, and brine diffusion of iodine biologically produced underneath and within porous sea-ice. It also includes heterogeneous recycling of inorganic halogen reservoirs deposited over fresh sea-ice surfaces and snow-covered regions. The polar emission of chlorine, bromine, and iodine reach approximately 32, 250, and 39 Gg/year for Antarctica and 33, 271, and 4 Gg/year for the Arctic, respectively, with a marked seasonal cycle mainly driven by sunlight and sea-ice coverage. Model results are validated against polar boundary layer measurements of ClO, BrO, and IO, and satellite BrO and IO columns. This validation includes satellite observations of IO over inner Antarctica for which an iodine "leapfrog" mechanism is proposed to transport active iodine from coastal source regions to the interior of the continent. The modeled chlorine and bromine polar sources represent up to 45% and 80% of the global biogenic VSL^{Cl} and VSL^{Br} emissions, respectively, while the Antarctic sea-ice iodine flux is ~10 times larger than that from the Southern Ocean. We present the first estimate of the contribution of polar halogen emissions to the global tropospheric halogen budget. CAM-Chem includes now a complete representation of halogen sources and chemistry from pole-to-pole and from the Earth's surface up to the stratopause.

Plain Language Summary We present the first implementation of an interactive polar module into the halogen version of the Community Atmosphere Model with Chemistry (CAM-Chem) model with the intention of expanding the model applicability to the polar regions, besides its wide usage for atmospheric studies throughout the tropics and midlatitudes. The state-of-the-art polar module considers full gas-phase and heterogeneous inorganic chlorine, bromine, and iodine chemistry and sources, which add up to the organic halogen emissions from the ocean surface (the so-called very short-lived substances, VSL). The online sea-ice halogen sources depend on the seasonal variation of different types of icy surfaces and the intensity of radiation reaching the polar surface. Our results indicate that the contribution of polar halogen sources represents between 45% and 80% of the global biogenic VSL chlorine and bromine emissions, respectively; and that the Antarctic iodine sea-ice annual flux is ~10 times larger than the total iodine source arising from the Southern Ocean. This work provides, for the first time, quantitative estimates of the annual and seasonal flux strength of each halogen family from the Arctic and Antarctic, as well as their contribution to the global tropospheric halogen budget, highlighting the importance of including the contribution of polar tropospheric halogens in global chemistry-climate models.

1. Introduction

The important role played by very short-lived (VSL) halogen chemistry on the global marine boundary layer (MBL) and its impact on ozone and other atmospheric oxidants, has been demonstrated both from experimental (e.g., Prados-Roman, Cuevas, Fernandez, et al., 2015; Read, Lewis, et al., 2008; Wang et al., 2015) and global modeling (e.g., Fernandez et al., 2014; Hossaini et al., 2010; Liang et al., 2010; Parrella et al., 2012; Saiz-Lopez, Lamarque, et al., 2012; Saiz-Lopez et al., 2014; Sherwen et al., 2016; Sinnhuber & Folkins, 2006; Yang et al., 2005) studies. VSL sources, through their degradation products, contribute to the tropospheric inorganic halogen loading throughout different geographical regions, expanding from the tropical areas (Aschmann et al., 2009; Saiz-Lopez & Fernandez, 2016) and midlatitudes (Mahajan et al., 2011; Parrella et al., 2012; Saiz-Lopez et al., 2014) to the polar regions (Pöhler et al., 2010; Raso et al., 2017; Saiz-Lopez et al., 2007, 2008; Simpson et al., 2007). The additional bromine released from VSL photodecomposition also leads to ozone depletion in the lowermost stratosphere (Dorf et al., 2008; Salawitch et al., 2005), estimating the additional stratospheric injection of VSL bromine to lie within the 5 (3–7) pptv range (WMO, 2018). Recently, the impact of VSL chemistry on the recovery of the Antarctic ozone hole has also been evaluated (Fernandez et al., 2017; Oman et al., 2016).

Halogen-mediated Ozone Depletion Events (ODEs) are persistent phenomena affecting the polar MBL both in the Arctic and Antarctica (e.g., Abbatt et al., 2012; Barrie et al., 1988; Bottenheim & Gallant, 1986; Jones et al., 2009; Martinez et al., 1999; Oltmans & Komhyr, 1986; Simpson et al., 2007; Sturges et al., 1993; Tuckermann et al., 1997). During these events, a very efficient recycling of inorganic bromine species (usually referred as bromine explosion) correlates with strong depletion of tropospheric ozone, reducing the O_3 mixing ratio to very small ambient levels, which in some cases lie below the instrumental detection limit (Simpson et al., 2007, 2015). Bromine oxide (BrO) plumes, that is, regional enhancements on the BrO tropospheric vertical column densities (VCDs), have been observed from different satellite platforms and are related to the occurrence of ODEs and bromine explosion events (Begoin et al., 2010; Theys et al., 2009, 2011). The role of chlorine on the generation of ODEs has also been widely studied (e.g., Abbatt et al., 2012; Liao et al., 2014; Saiz-Lopez & von Glasow, 2012).

Both ice and snow have been recognized as important sources of reactive halogen species to the polar atmosphere. The photochemical heterogeneous production of reactive bromine and chlorine occurring at the sea-ice and snowpack surface have been suggested as a very efficient mechanism to release the enhanced halide content prevailing over ice-covered regions (Abbatt et al., 2012; Dominé & Shepson, 2002; Foster et al., 2001; Pratt et al., 2013; Wang & Pratt, 2017; Yang et al., 2010). Additionally, the biologically induced release of inorganic iodine (and possibly bromine) from underneath the sea-ice followed by brine diffusion (Saiz-Lopez, Boxe, et al., 2015) can represent the dominant source of iodine (and a nonnegligible source of bromine) to the polar MBL. Likewise, efficient mechanisms of halogen activation of reservoir species occurring on environmental ice and snow have been proposed to represent additional sources (Falk & Sinnhuber, 2018; Kim et al., 2016, 2019; O'Driscoll et al., 2006; O'Sullivan & Sodeau, 2010; Toyota et al., 2011). Equivalent recycling reactions occur also on sea-salt aerosols (Fernandez et al., 2014; McFiggans et al., 2000; Vogt et al., 1996). Some of these recycling processes are proposed to be controlled by ozone deposition with subsequent halide oxidation (Artiglia et al., 2017; Liao et al., 2014; Toyota et al., 2011). Unlike bromine and chlorine, the much smaller atmospheric iodine levels observed in the Arctic with respect to the Antarctic, results in a "polar iodine paradox," which is not yet fully understood (Saiz-Lopez & Blaszczak-Boxe, 2016).

Within the polar regions, oceanic emissions of VSL halocarbons are insufficient to account for the high concentrations of gas-phase iodine and bromine observed in the MBL (Pöhler et al., 2010; Saiz-Lopez, Plane, et al., 2012; Simpson et al., 2015). For the case of iodine, in addition to the biological VSL iodocarbon source, an abiotic inorganic iodine release from the ocean surface occurs (Carpenter et al., 2013; MacDonald et al., 2014; Prados-Roman, Cuevas, Fernandez, et al., 2015). These inorganic iodine sources arising from the polar oceans are not sufficient to reproduce the measured iodine levels at different Arctic and Antarctic sites (Atkinson et al., 2012; Mahajan, Shaw, et al., 2010; Saiz-Lopez et al., 2007). Thus, additional sources from the sea-ice surface, and/or transported from underneath the sea-ice, must be considered in order to reproduce the halogen burden in the polar troposphere.

Box- and 1-D-modeling studies have been used to evaluate and describe the role of bromine explosion events on the occurrence of Arctic and Antarctic ODEs (Jones et al., 2009; Lehrer et al., 2004; Liao et al., 2014; Saiz-Lopez et al., 2008; Thompson et al., 2015), as well as other oxidative impacts of halogens on mercury, OH/HO_2, NO/NO_2, and dimethyl sulfide occurring in the polar regions (Bloss et al., 2010; Brooks et al., 2006; Evans, 2003; Goodsite et al., 2004; Mahajan, Shaw, et al., 2010; Pöhler et al., 2010; Read, Mahajan, et al., 2008; Skov et al., 2004; Steffen et al., 2007). However, global Chemistry-Climate Models (CCMs) and Chemical Transport Models (CTMs) do not currently include the contribution of full tropospheric halogen sources and chemistry over the polar regions (Fernandez et al., 2017; Hossaini et al., 2016; Liang et al., 2014; Parrella et al., 2012; Sherwen et al., 2016), which may produce a nonnegligible bias on simulations of the global tropospheric ozone burden. A few attempts have been performed to implement halogen polar emissions in CTMs/CCMs (Falk & Sinnhuber, 2018; Toyota et al., 2011; Yang et al., 2010), although these studies only focused on bromine sources and included a simplified and unique approach to represent the different processes that lead to polar halogen emissions from the sea-ice surface.

Here we present the first fully consistent pole-to-pole tropospheric VSL halogen (Cl, Br, and I) chemistry scheme, considering (i) global emissions of VSL halocarbons from the ocean as well as release of inorganic halogens both from the ocean and from ice-covered areas within both polar regions; (ii) a state-of-the-art gas- and heterogeneous-phase halogen chemical mechanism, including reactive and reservoir chlorine, bromine, and iodine species; and (iii) production from sea-salt aerosols, formation of liquid and ice clouds and precipitation, as well as individual dry/wet deposition for relevant halogen species at the surface level and throughout the troposphere. The additional sea-ice sources have been included interactively into an *online polar module* representing the photochemical production of bromine and chlorine, the brine diffusion of reactive iodine biologically produced underneath the sea-ice, as well as the recycling of inorganic halogens deposited over ice-covered areas (distinguishing between different types of sea-ice and snowpack) and sea-salt aerosols. The model results are validated against ground- and satellite-based observations of halogen species in the Arctic and Antarctica. We also quantify for the first time the overall contribution of polar halogen emissions to the global halogen budget.

The paper is structured as follows: Section 2 presents the benchmark Community Atmosphere Model with Chemistry (CAM-Chem) configuration used in this study, the observational data used for validation, and the full set of experiments performed to evaluate the new model performance. Section 3 describes each of the emission sources included in the polar module and how they were parameterized into the CAM-Chem global CCM. This section also provides a brief description of the main geophysical factors influencing the spatial and temporal evolution of the implemented sea-ice emissions. Section 4 places emphasis on evaluating the model performance for the different experiments and validates surface and tropospheric levels of halogen oxides against observations performed both in the Arctic and Antarctica. Quantitative estimations of the annual flux strength, distribution, and seasonal variation of the sea-ice sources within each polar region, as well as a comparison to the benchmark VSL global sources, are presented in section 5. Finally, discussions of the main implications of fully considering polar tropospheric halogen emissions and chemistry in a global CCM, as well as the main conclusions of the work, are summarized in section 6.

2. Materials and Methods

2.1. CAM-Chem Benchmark VSL Halogen Configuration

The novel interactive polar module has been incorporated into the VSL halogen (Cl, Br, and I) version of the CAM-Chem (Fernandez et al., 2014; Ordóñez et al., 2012; Saiz-Lopez et al., 2014), which constitutes the atmospheric component of the Community Earth System Model framework (CESM, Lamarque et al., 2012; Tilmes et al., 2016). The VSL halogen setup includes a state-of-the-art halogen chemical scheme, including 296 total gas-phase inorganic reactions (192 for halogen species, denoted by X and/or Y throughout the text), 33 heterogeneous reactions occurring on sea salt, sulfate, nitrate, and carbonaceous aerosols (19 halogen reactions), and a complete scheme of gas-phase organic chemistry (145 reactions, 19 for halogens) based on Emmons et al. (2010). The implementation and validation of VSL oceanic emissions in the model has been provided by Ordóñez et al. (2012), while Prados-Roman, Cuevas, Fernandez, et al. (2015)

described the online computation of inorganic iodine oceanic sources arising from the ozone-mediated oxidation of surface seawater iodide. Further descriptions of the VSL halogen mechanism implemented in CAM-Chem can be found elsewhere (Cuevas et al., 2018; Fernandez et al., 2014, 2017; Navarro et al., 2015, 2017; Saiz-Lopez et al., 2014; Saiz-Lopez, Baidar, et al., 2015).

Within the lower boundary, zonally averaged distributions of greenhouse gases as well as long-lived halocarbons are specified following their observed surface concentration for the year 2000 (Meinshausen et al., 2011). To avoid dynamical perturbations and to allow a multiple model experiments intercomparison, prescribed climatological sea surface temperatures and sea-ice extent distributions for the 2000th decade (i.e., between 1995 and 2005) were also considered (Rayner, 2003). Note that all of these prescribed fields have monthly resolution, allowing the computation of the sea-ice seasonal changes within 1 year, which are repeated iteratively year after year. Photolysis rate constants are computed online considering both a look-up table and CAM-Chem actinic flux calculations (Lamarque et al., 2012). The stratospheric halogen chemistry in the model is based on Kinnison et al. (2007) and Wegner et al. (2013) and has been widely described elsewhere (Fernandez et al., 2014, 2017; Lamarque et al., 2012). All rate constants have been updated to JPL-2010 (Jet Propulsion Laboratory, Sander et al., 2010, 2011) and IUPAC-2008 (International Union of Pure and Applied Chemistry; Atkinson et al., 2007, 2008).

In this work, all simulations were performed with a horizontal resolution of 1.9° latitude by 2.5° longitude and 26 vertical levels, from the surface up to ~3 hPa (~40 km), running in specified dynamics mode. The model is forced by high-frequency meteorological and dynamical fields obtained from a previous CAM-Chem 15-year free-running simulation, including the full VSL halogen scheme, but without the polar module (Fernandez et al., 2014; Saiz-Lopez et al., 2014). Thus, the CAM-Chem configuration used here only solves for the chemical evolution of the atmosphere while forcing the model to a consistent but fixed meteorological evolution of the troposphere, which in turn is based on prescribed ocean and ice coverage fields that remain identical for all the experiments performed. This nudged setup is preferred for implementing new model developments and parameterizations, in order to isolate the chemically and source-driven changes from those driven by atmospheric dynamics (Fernandez et al., 2014; Saiz-Lopez et al., 2014; Saiz-Lopez & Fernandez, 2016). Note that simulations do not pertain to any specific year but are representative of the 2000th decade.

The benchmark VSL halogen setup includes also the contribution of sea-salt aerosol (SSA) recycling. Sea-salt aerosols are generated by breaking waves on the ocean surface (Monahan et al., 1986; Smith et al., 1993) and can be transported well above the MBL where their washout efficiency decreases (Murphy et al., 2018). Heterogeneous halogen reactions taking place on the surface of SSA have previously been included in CAM-Chem for HX, HOX, and $XONO_2$ species (Fernandez et al., 2014; Ordóñez et al., 2012), based on the assumption that the rate-limiting step for the heterogeneous recycling reaction is the uptake of the inorganic halogen species on the aerosol surface (McFiggans et al., 2000). The aproach assumes that the sea-salt aerosol bulk constitutes an infinite pool of chloride and bromide, which is large enough for the heterogeneous reactions to occur until the sea-salt aerosol is removed by depositional processes. This is justified considering that the mean lifetime of sea-salt aerosols within the model is less than 1 day (Lamarque et al., 2012; Mahowald et al., 2006); thus, SSA is daily renewed with fresh and halide rich sea-salt aerosol. Additionally, we imposed a vertical mask to the recycling mechanism above ~300 hPa (~8–9 km) to avoid the SSA dehalogenation computation at high altitudes where it is most probable that aged sea-salt aerosols would prevail (Fernandez et al., 2014). The three-dimensional SSA recycling parameterization follow a different approach to the sea-ice surface flux and has been implemented within the main chemical driver instead of constituting a typical additional surface source within the emissions routines.

2.2. Observations Used for Validation

Figure S1 in the supporting information shows the location of each of the Arctic and Antarctic stations whose atmospheric surface observations are considered in this study. The period of time when each campaign took place as well as the measurement technique employed are summarized in Table S1. Most of these measurements were made by the Differential Optical Absorption Spectroscopy (DOAS) technique (Plane & Saiz-Lopez, 2006; Platt & Stutz, 2008), measuring the structured absorption bands of BrO and ClO in the Ultraviolet (UV) region of the spectrum, and IO in the Visible (Vis) region. This technique

uses an artificial light source in the case of Long-Path DOAS (LP-DOAS), and scattered sunlight in the Multi-Axes DOAS (MAX-DOAS) configuration. Other BrO measurements, for instance, those by Liao et al. (2012), were made at Barrow, Alaska, by Chemical Ionization Mass Spectrometry.

Satellite data from the space borne UV-Vis sensors SCIAMACHY (Scanning Imaging Absorption spectroMeter for Atmospheric CHartographY; Bovensmann et al., 1999; Burrows et al., 1995) and GOME-2A (Global Ozone Monitoring Experiment-2A; Callies et al., 2000) have been used for model validation. SCIAMACHY onboard the European Space Agency Envisat satellite and GOME-2A onboard the European Space Agency/EUMETSAT MetOp-A satellite are in Sun-synchronous orbits with equator-crossing times of 10:00 a.m. and 09:30 a.m., respectively. The instruments record the backscattered radiance from Earth in nadir direction as well as the direct solar irradiance. Alternative viewing modes such as limb and occultation for SCIAMACHY are not used here. Monthly mean climatology averaged between 2007–2012 for BrO and 2004–2011 for IO have been used in this study. While GOME-2A is still in operation, SCIAMACHY stopped measuring in April 2012.

Total slant column densities (SCDs) of IO from SCIAMACHY nadir data and of BrO from GOME-2A data are retrieved using the DOAS method (Platt, 1994). IO is retrieved in the visible spectral range from 416–430 nm (Schönhardt et al., 2008) and BrO in the UV range 336–347 nm (Afe et al., 2004; Begoin et al., 2010). A cloud screening algorithm is not used here for both, IO and BrO, as the detection of clouds over snow and ice from satellite is challenging. As IO column amounts are comparably small and close to the detection limit, an average Earthshine spectrum is used as reference background in the IO retrieval in order to improve the signal-to-noise-ratio. The selected reference region is located in the remote Pacific (30–50°S and 150–170°W) were IO amounts are assumed to be close to zero. This has been verified in an alternative retrieval with solar reference. Since no IO is expected in the stratosphere, no stratospheric correction method is applied and the retrieved total column may be used as tropospheric slant column.

The conversion of tropospheric SCDs of IO to VCDs is done by application of a tropospheric air mass factor that implicitly assumes that IO is well mixed within the lowest few hundred meters over snow and ice with a constant albedo of 0.9 (Schönhardt et al., 2008). Outside snow- and ice-covered regions (e.g., over the predominantly dark ocean), tropospheric IO amounts would therefore be underestimated, which is important to note when comparing satellite retrievals to model simulations. The derivation of tropospheric VCDs of BrO is more complicated, as significant amounts of BrO also occur in the stratosphere so that the stratospheric component has to be subtracted from the total column. In the present manuscript, due to constraints in deriving tropospheric BrO for specific time periods over Antarctica, satellite-derived geometric VCDs of BrO are compared to total VCDs of BrO simulated by CAM-Chem for both the Arctic and Antarctica. Geometric VCDs of BrO are derived by application of a stratospheric air mass factor to retrieved total SCDs. Geometric VCDs are expected to be closer to total VCDs over regions with high surface albedo (snow- and ice-covered areas) but will underestimate total VCDs over the open ocean, mainly due to an underestimation of the tropospheric part of the total column. For further details on the retrievals, the reader is referred to Schönhardt et al. (2008, 2012) for IO, as well as to Blechschmidt et al. (2016) and Begoin et al. (2010) for BrO.

2.3. Model Experiments

Two independent CAM-Chem model experiments, with ($VSL^{\text{PM-on}}$) and without ($VSL^{\text{PM-off}}$) polar emissions, were performed to evaluate the loading of tropospheric halogens in the polar troposphere. Each of the model experiments was run for 3 years starting from identical initial and boundary conditions (see section 2.1), and the output from the last year of simulation was used. Within the full pole-to-pole setup, an additional run was designed by turning off the direct sea-ice sources (i.e., those described in section 3.2) with the intention of evaluating the effectiveness of the heterogeneous recycling of deposited reservoir species (i.e., those described in section 3.3) whenever the initial photochemical release of gas-phase halogens from the sea-ice surface is not considered ($VSL^{\text{PM-ind}}$). This multiple experiments inter-comparison allows a quantitative evaluation of the improvements in the representation of halogen chemistry within the polar regions.

Validation of a global CCM like CAM-Chem against surface measurements is not straightforward, as the vertical extent of the lowest level of the model is on the order of 100–300 m, depending on the model
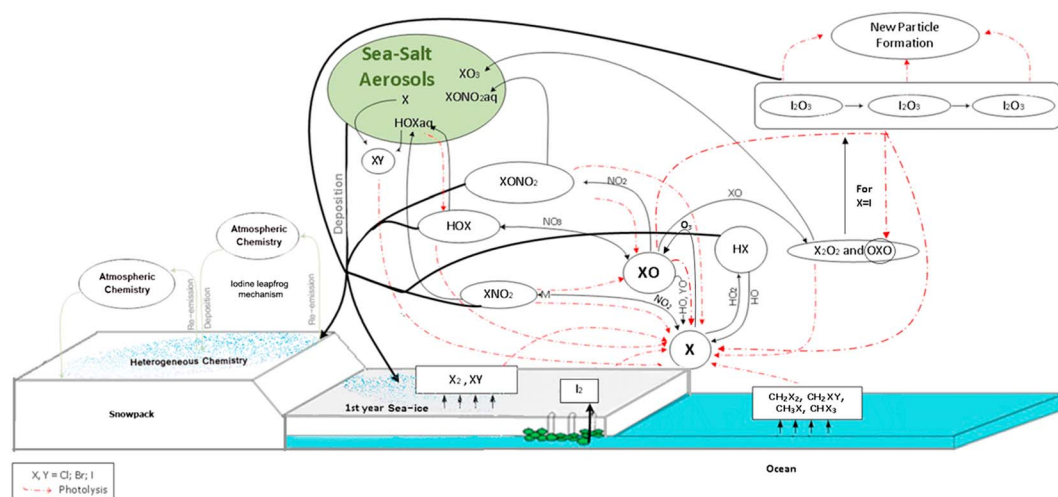
Figure 1. Schematic representation of the polar halogen sources as well as the gas-phase and heterogeneous-phase chemistry implemented in the CAM-Chem polar module. Red-dashed arrows represent photochemical processes, while solid thin black arrows represent bimolecular and termolecular reactions. Sea-salt aerosols are highlighted with a green background, while the halogenated reservoirs capable of being deposited and recycled on the sea-ice surface are encircled by an empty ellipse and connected by solid thick arrows.

resolution and configuration. Thus, in order to compare CAM-Chem output with atmospheric surface measurements (e.g., BrO and IO), we have employed simulations from the THAMO model for typical polar conditions to determine the vertical distribution of gas-phase species within the MBL. THAMO is a 1-D chemistry transport model with 200 stacked boxes at a vertical resolution of 5 m (total height 1 km). The model treats iodine, bromine, O_3, NO_x, and HO_x chemistry and is constrained with typical measured values of other chemical species in the MBL (Saiz-Lopez et al., 2008). The model is initialized at midnight and the evolution of iodine species, O_3, NO_x, and HO_x is followed until the model reaches steady state. THAMO has been used in previous works to study tropospheric halogen chemistry in different locations, including polar and midlatitude environments. Further details, including the full chemical scheme, can be found elsewhere (Lawler et al., 2014; Mahajan, Shaw, et al., 2010; Mahajan, Plane, et al., 2010; Saiz-Lopez et al., 2008). A scaling factor between the CAM-Chem (low-resolution) and THAMO (high-resolution) vertical profiles can be obtained by nonlinear regression between 0- and 1-km altitude. This scaling factor can then be used to extrapolate the CAM-Chem output at the same altitude at which the measurements were performed. Individual scaling factors for BrO and IO are provided in the supporting information (Table S2). Due to the lack of a vertical profile of ClO in the literature, the ClO factor has been calculated from an estimated THAMO ClO vertical profile based on the relation between the BrO and ClO vertical profiles from CAM-Chem in the troposphere.

3. Implementation of the Halogen Polar Module in CAM-Chem

Figure 1 depicts the different chemical processes that compose the polar-module coupled to the CAM-Chem halogen core: (i) emissions of inorganic halogens either by photochemical oxidation of halide reservoirs at the sea-ice surface or due to the biological production by microalgae activity below the thin sea-ice followed by brine diffusion; (ii) deposition of gas-phase reservoirs and re-emission of inorganic chlorine, bromine, and iodine from first-year sea-ice and fresh snow covering the polar continents or multiyear sea-ice; and (iii) uptake and recycling of inorganic halogens from sea-salt aerosol, which enhances the total flux of halogens to the lower troposphere over coastal areas. Even though the overall recycling mechanism leading to the uptake and release of halogens from the sea-ice surface to the atmosphere is quite complex, here we have split the different types of processes as follows: direct photochemical sources are computed at the sea-ice surface and occur independently of the prior existence of an initial gas-phase halogenated molecule within the lower boundary of the model; while the induced heterogeneous recycling source requires the prior existence of a gas-phase halogenated reservoir that deposits on the sea-ice and/or aerosol surface and, through
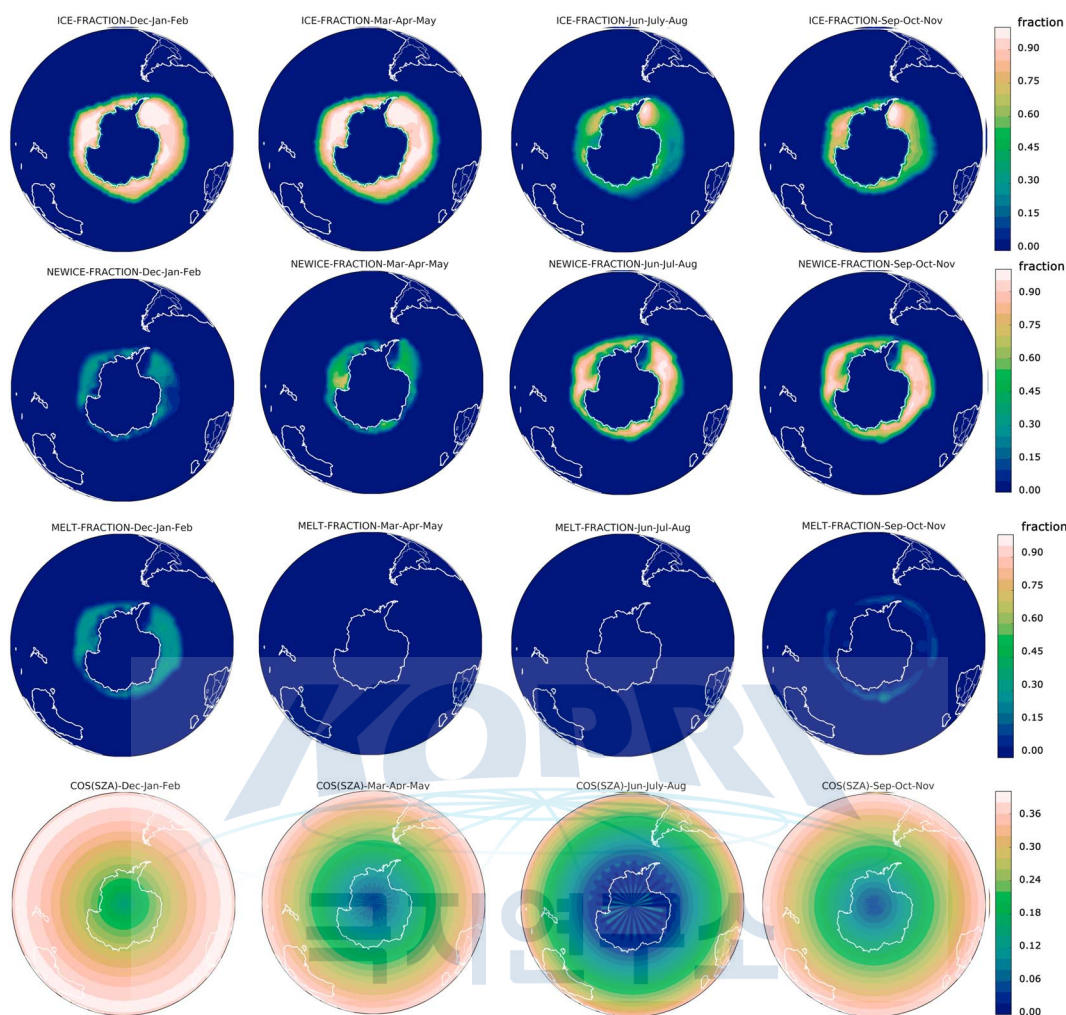
Figure 2. Geographical distribution of the main geophysical variables affecting Antarctic sea-ice emissions: (first row) multiyear sea-ice (icefrac); (second row) first-year sea-ice (newice); (third row) meltice; and (fourth row) intensity of radiation (cos *(SZA)*). Each independent panel on each row represents the seasonal mean of each geophysical variable.

heterogeneous halide reactions, leads to the release of an additional halogen molecule back to the atmosphere.

3.1. Geophysical Drivers Affecting Polar Sea-Ice Emissions

The polar halogen emissions are computed considering the seasonal changes of different types of sea-ice surfaces covering the polar regions of the Northern (NH) and Southern (SH) Hemispheres: multiyear sea-ice (*icefrac*), defined as the total fraction of a model grid point that is covered by sea-ice; first-year sea-ice (*newice*), defined as the fraction of the multiyear sea-ice that is renewed every year with fresh sea-ice since its minimum summer extent; the continental *snowpack*, representing those continental grid points that are covered by ice; and an additional parameter called *meltice* representing the fraction of first-year sea-ice that has been thawed out during the last month since its maximum winter extent. Additionally, the polar sources depend on the net solar irradiance reaching the Earth's surface at each latitude, longitude, and time of day for each season (i.e., dependent on the cosine of Solar Zenith Angle, cos (*SZA*)), as well as the depositional flux of individual inorganic halogen reservoirs on the surface of the sea ice/snowpack and/or its uptake on sea-salt aerosols occurring both during the day and at night.

Figures 2 and 3 show the spatial distribution of the main geophysical variables driving polar halogen emissions. The first two rows highlight the very different distribution of sea-ice extent prevailing in the NH and SH: while the Arctic sea-ice coverage is centered on the North Pole and maintains an innermost core with
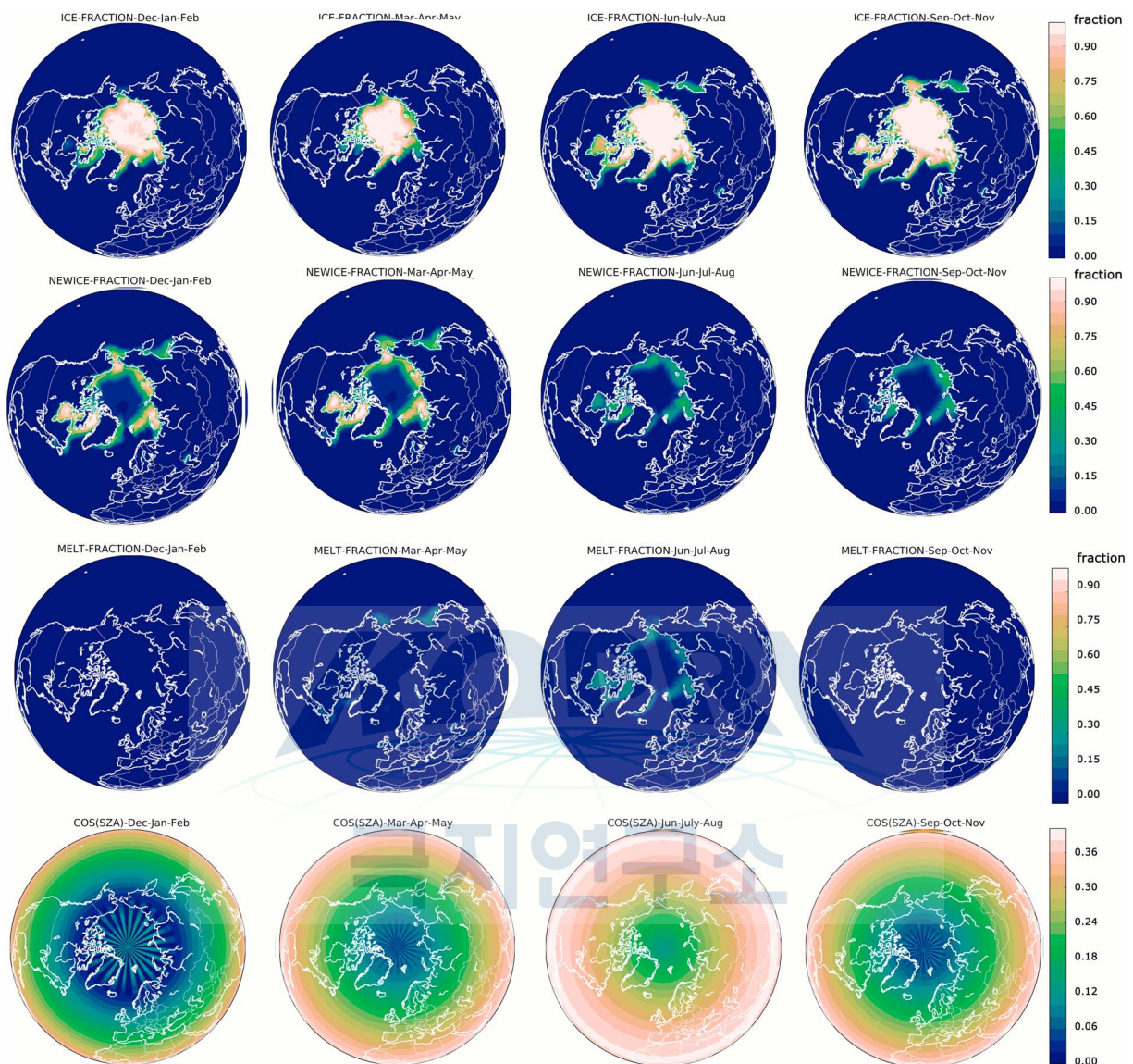
Figure 3. Same as Figure 2 but for the Arctic.

complete ice coverage throughout the annual seasonal cycle (ice fraction > 0.9), the SH sea-ice surrounding the Antarctic continent is renewed every year (showing ice fractions smaller than 0.5 during the summer) with the exception of some local features located on the Weddell and Ross seas. This indicates that mostly multiyear (i.e., aged, compactedand thick) sea-ice prevails in the NH (first row in Figure 3); while young, thing and porous first-year sea-ice encircles Antarctica at most locations (second row in Figure 2). The mel-tice parameter (third row on Figures 2 and 3) shows a completely different seasonal variation compared to icefrac and newice, with larger distributions prevailing during the summer months in both hemispheres. Additionally, the seasonal variation of cos (SZA), representative of the mean irradiance reaching high latitudes during each season (fourth row in Figures 2 and 3), indicates that during the winter less than 30% of the mean radiation available in the tropics reaches the polar regions (showing a latitudinal variation that minimizes at each pole). During the summer, up to 70% (60%) of the net irradiance present in the tropics reaches the icy surfaces over Antarctica (the Arctic).

To highlight how the seasonal variation of these geographical factors can impact on the sea-ice flux parame-terizations, Figure 4 presents the spatially averaged monthly mean for each sea-ice extent definition and for cos (SZA), as well as the normalized product of these variables. Note that the product of the sea-ice area × cos
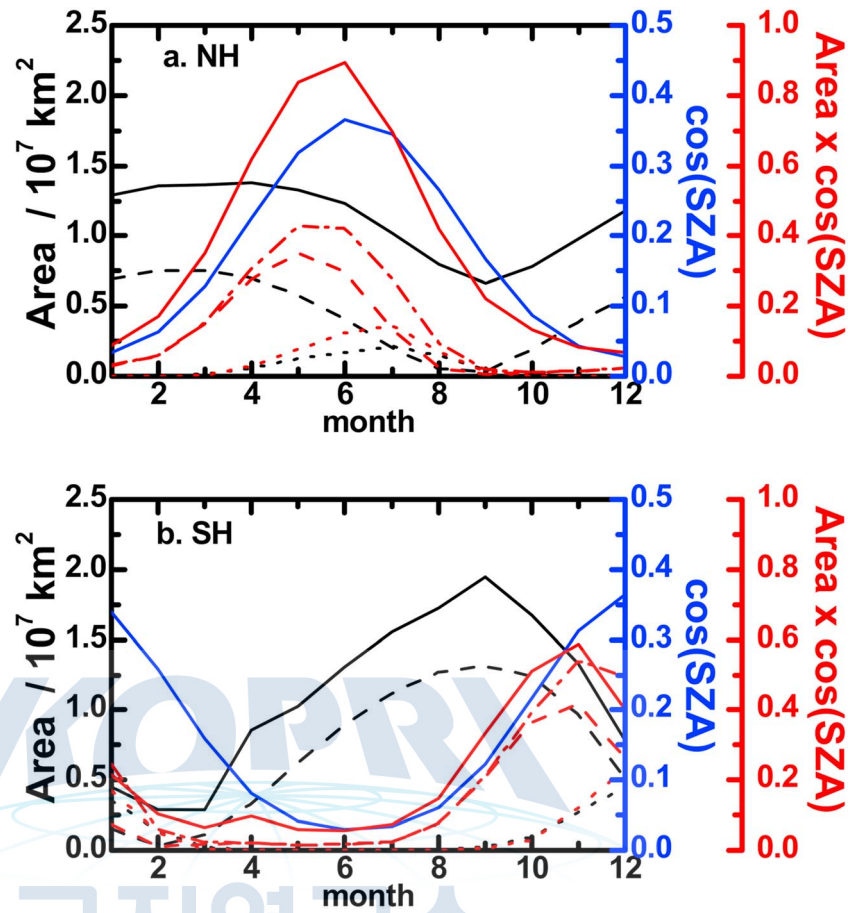
Figure 4. Annual seasonal cycle of the main geophysical variables affecting the source strength of each halogen source within the Arctic (top) and Antarctica (bottom). The left axis (black) presents the total icefraction (solid), newice (dashed), and meltice (dotted) area integrated within each polar cap, while the innermost right axis (blue) shows the monthly mean cos *(SZA)*, representing the intensity of radiation within each polar region. The outermost right axis (red) shows the normalized product of both magnitudes (area$_{sea\text{-}ice}$ × cos *(SZA)*) for each of the sea-ice extent definitions. The dash-dotted red line is the sum of the normalized product for area$_{meltice+newice}$ × cos (SZA).

(SZA) follows the shape of the intensity of radiation reaching the polar surface on each hemisphere (blue line), but that the seasonality of this product has a phase shift depending on the consideration of multiyear (solid line), first-year (dashed line) or *meltice* (dotted) extent. As described below, the geographical and temporal superposition of these two features determines the dominant pattern of the total halogen emission in the polar regions.

3.2. Photochemical Release of Reactive Halogens From the Sea-Ice Surface

Equation (1) represents the bromine and chlorine flux from the photochemical oxidation of the halide content prevailing at the sea-ice surface. The initial bromide and chloride enrichment existent on top of the thin brine layer is assumed to be maintained either by the physicochemical liquation of salty water during the sea-ice solidification or through the deposition of halogen rich sea-salt aerosols (Abbatt et al., 2012; Saiz-Lopez & von Glasow, 2012). Within the model, we assume that the initial bromide and chloride pool on the sea-ice is infinitely large (i.e., the fresh sea-ice constitutes a nonexhaustible halide reservoir). Thus, the time-dependent surface flux must be adjusted to respond to the main geophysical parameters controlling the photo-oxidative process.

$$F_{\text{ICE}}^{\text{XY}}(i,t) = F_0 \times R_{XY} \times H_{\text{N/S}} \times \frac{(\text{newice}(i) + \text{meltice}(i))}{\text{max}_{\text{ICE}}} \times \frac{\cos(SZA(i,t))}{\text{max}_{\text{SZA}}} \tag{1}$$

Table 1
Photochemical Sea-Ice Emissions Implemented in the CAM-Chem Polar Module

Sea-ice flux expression based on equations (1)[a] and (2)[b]	Adjusted parameter[c]
$F_{ICE}^{Cl2}(i,t) = F_0 \times R_{XY} \times H_{N/S} \times \frac{(newice(i)+meltice(i))}{max_{ICE}} \times \frac{cos(SZA(i,t))}{max_{SZA}}$	$F_0 = 1.0\times10^9$; $R_{XY} = {}^{1}\!/_{4}$; $H_{N/S} = 0.4$; $\begin{cases} max_{ICE} = 0.63 \\ max_{SZA} = 0.50 \end{cases}$
	$F_0 = 1.0\times10^9$; $R_{XY} = {}^{1}\!/_{4}$; $H_{N/S} = 0.4$; $\begin{cases} max_{ICE} = 0.88 \\ max_{SZA} = 0.50 \end{cases}$
$F_{ICE}^{BrCl}(i,t) = F_0 \times R_{XY} \times H_{N/S} \times \frac{(newice(i)+meltice(i))}{max_{ICE}} \times \frac{cos(SZA(i,t))}{max_{SZA}}$	$F_0 = 1.0\times10^9$; $R_{XY} = {}^{1}\!/_{2}$; $H_{N/S} = 0.4$; $\begin{cases} max_{ICE} = 0.63 \\ max_{SZA} = 0.50 \end{cases}$
	$F_0 = 1.0\times10^9$; $R_{XY} = {}^{1}\!/_{2}$; $H_{N/S} = 0.4$; $\begin{cases} max_{ICE} = 0.88 \\ max_{SZA} = 0.50 \end{cases}$
$F_{ICE}^{Br2}(i,t) = F_0 \times R_{XY} \times H_{N/S} \times \frac{(newice(i)+meltice(i))}{max_{ICE}} \times \frac{cos(SZA(i,t))}{max_{SZA}}$	$F_0 = 1.0\times10^9$; $R_{XY} = {}^{5}\!/_{4}$; $H_{N/S} = 0.6$; $\begin{cases} max_{ICE} = 0.63 \\ max_{SZA} = 0.50 \end{cases}$
	$F_0 = 1.0\times10^9$; $R_{XY} = {}^{5}\!/_{4}$; $H_{N/S} = 0.5$; $\begin{cases} max_{ICE} = 0.88 \\ max_{SZA} = 0.50 \end{cases}$
$F_{ICE}^{I2}(i,t) = F_0 \times H_{N/S} \times chl_a(i) \times \frac{cos(SZA(i,t))}{max_{SZA}}$	$F_0 = 1.7\times10^9$; $max_{SZA} = 0.50$; $\begin{cases} H_{N/S} = 0.01 \\ \text{if}(\,cos(SZA)\geq0.6) \to cos(SZA) = 0.6 \end{cases}$
	$F_0 = 1.7\times10^9$; $max_{SZA} = 0.50$; $\begin{cases} H_{N/S} = 0.4 \\ \text{if}(\,cos(SZA)\geq0.6) \to cos(SZA) = 0.6 \\ \text{if}(icefrac\geq0.85) \to H_{N/S} = 1.0 \end{cases}$

[a]The left column of the table presents the individual expressions for each halogen species emitted from the sea-ice surface based on equation (1). F_0 is the initial surface flux for each halogen species; $H_{N/S}$ is a hemispheric factor; newice(i) and icefrac(i) are the first-year and multiyear sea-ice fractions, respectively, at a given model grid point; cos (SZA(i,t)) is the cosine of the SZA at each model grid point and time of the day; max_{ICE} and max_{SZA} are the adjusted maximum sea-ice extent and radiation imposed to normalize the emission strength. See the text for further details. [b]The F_{ICE} expression for I_2 is computed only when icefrac(i) > 0 and meltice(i) < 0.15. $chl_a(i)$ is a monthly dependent chlorophyll-a map from the Giovanni data portal used as proxy for the biological activity underneath the sea-ice. [c]The adjusted parameters for each expression in the left column are provided for the NH (top) and SH (bottom) lines within each row. Units for F_0 are molec·cm^{-2}·s^{-1}. All the remaining parameters are dimensionless and represent relative fractions between 0 (zero) and 1 (one).

Here we parameterized the sea-ice flux (F_{ICE}^{XY}) at each model gridpoint and time (*i,t*) considering (i) the fraction of first-year sea-ice prevailing at each location (*newice(i)* and *meltice(i)*) with respect to the maximum sea-ice extent on each polar region during the year (*max_ICE*); and (ii) the intensity of radiation reaching the sea-ice surface at each time of day (represented by cos *(SZA(i,t))*) normalized by the maximum radiation (*max_SZA*) reaching the Arctic or Antarctica throughout the year. As the bromine and chlorine emissions are abiotic, they only respond to the geographical changes of the *newice(i)*, *meltice(i)*, and cos *(SZA(i,t))* variables (see Table 1). F_0 is the initial baseline flux, originally taken from a 1-D model of BrO concentrations in Antarctica (Saiz-Lopez et al., 2008), which was iteratively adjusted to improve the CAM-Chem agreement with surface and satellite measurements. $H_{N/S}$ is a hemispheric factor which represents the different chloride and bromide content prevailing in the Arctic and Antarctica, and relates the efficiency of the process between both polar regions. All of the Arctic and Antarctic parameters provided in Table 1 have been adjusted by comparing model results and observations in an iterative manner (following a bottom-up approach), and they are related with the different physical (*max_ICE*), chemical (*H_N/S*) and radiative (*max_SZA*) properties (e.g., sea-ice thickness, ocean salinity, and precipitation, see Yang et al., 2010). Note that the polar module includes the initial sea-ice flux of bromine and chlorine in the form of Br$_2$ (F_{ICE}^{Br2}), BrCl (F_{ICE}^{BrCl}), and Cl$_2$ (F_{ICE}^{Cl2}, see Table 1). Cl$_2$ emission also takes place in the polar atmosphere (Liao et al., 2014) and can be rapidly recycled to and from BrCl at the sea-ice surface and/or snow (Foster et al., 2001; Wang & Pratt, 2017). Thus, once the F_0 value was adjusted for Br$_2$ and Cl$_2$, we compute the final F_{ICE} flux

by introducing a halogen-species interconversion factor (R_{XY}) representing the fraction of bromine and chlorine atoms being released from the sea-ice surface as Br_2, Cl_2, and BrCl (see Table 1).

Macroalgae and microalgae production of aqueous iodide (I^-_{aq}) and hypoiodous acid (HOI) occurring within and below the first-year sea-ice, followed by the reactive diffusion through sea-ice brine channels and release to the atmosphere (Saiz-Lopez, Boxe, et al., 2015), has been suggested as one of the possible main sources of iodine required to reproduce the high concentrations of iodine oxides observed in coastal Antarctica (Saiz-Lopez et al., 2007). This biologically induced flux of I_2 (and to a lesser extent IBr and/or ICl which are not considered here), can filter throughout the porous sea-ice coverage and reach the polar atmosphere. A mechanism considering the depth-dependent diffusion time scale, the liquid/gas phase equilibrium of halogen species, the temperature gradient between the lower atmosphere and the sea-ice surface underneath, as well as the photochemical diurnal and sea-ice thickness dependence, has been described by means of implementing a detailed multiphase model (Saiz-Lopez, Boxe, et al., 2015). In order to implement such a complex mechanism within CAM-Chem, we have simplified the main assumptions and parameterized the emission flux only for gas phase I_2 released to the atmosphere from the sea-ice surface (F^{I2}_{ICE}) as follows:

$$F^{I2}_{ICE}(i, t) = F_0 \times H_{N/S} \times chl_a(i) \times \frac{\cos(SZA(i,t))}{\max_{SZA}} \qquad (2)$$

where F_0 is the maximum possible I_2 flux computed for the baseline Antarctic conditions in Saiz-Lopez, Boxe, et al. (2015); $chl_a(i)$ is a monthly dependent chlorophyll-a map used as proxy for the biological activity underneath the sea-ice, and the remaining parameters are equivalent to the ones described for equation (1). Note that even though equation (2) does not include explicitly any sea-ice term, the expression is only computed for model grid points with small *meltice* values and a differentiated efficiency dependent on the *icefrac* extent (see Table 1), which implies that the parameterized iodine emission only occurs when polar sea-ice is breaking apart and thinning out. The chl_a maps have been obtained from the Giovanni data portal (https://giovanni.gsfc.nasa.gov/giovanni/) with monthly seasonal distributions. Because these maps are incapable of assigning a biological activity proxy below completely ice-covered regions, we modified the Giovanni chl_a maps within regions with large year-round icefractions (such as the Weddell and Ross seas) by imposing the values prevailing on the nearest non ice-covered grid ponts. The implemented iodine sea-ice flux requires a minimum threshold of radiation reaching the sea-ice surface to begin but rapidly saturates and becomes independent on the intensity of radiation. Thus, we imposed a cos *(SZA)* cap to the F^{I2}_{ICE} expression as indicated in Table 1.

A qualitative illustration of the very different behavior of the total sea-ice source throughout the seasonal cycle, as well as its dependence on the geophysical variables described in section 3.1, is presented in Figures 5 and 6. Note that in these panels both the contribution of the photochemical (F_{ICE}, section 3.2) and heterogeneous (F_{HET}, Section 3.3) sea-ice fluxes is considered ($F_{POLAR} = F_{ICE} + F_{HET}$), and that the source strength for the three months considered in each season has been added (Figures S2 and S3 in the supporting information show equivalent results considering only the photochemical F_{ICE} source). Most notably, the sea-ice flux for chlorine and bromine maximize during boreal summer in the Arctic since the intensity of radiation peaks during this season while at the same time, large fractions of the Arctic first-year sea-ice covered areas remain frozen. In contrast, the sea-ice flux in Antarctica maximizes during austral spring because during this season the sea-ice extent is still large and only starting to decrease, while at the same time the intensity of radiation is rapidly increasing each day moving into the austral summer (Figure 4). Because the dominant sea-ice extent in Antarctica is located at comparatively lower latitudes with respect to the Arctic, the superposition of maximum summertime surface irradiance with first-year sea-ice extent is considerably reduced, and thus smaller emissions are modeled to occur. During the boreal winter, there are nonnegligible emissions at low-latitudes (e.g., close to the Arctic polar circle), where the maximum wintertime Arctic fresh sea-ice extent reaches regions with non-null surface irradiance (see Figure S3 in the supporting information).

3.3. Heterogeneous Recycling of Reservoir Species Deposited on the Sea-Ice

The implementation of the heterogeneous recycling of halogenated reservoir species deposited on top of the sea-ice follows the original mechanism described by Fan and Jacob (1992) and Foster et al. (2001), which has
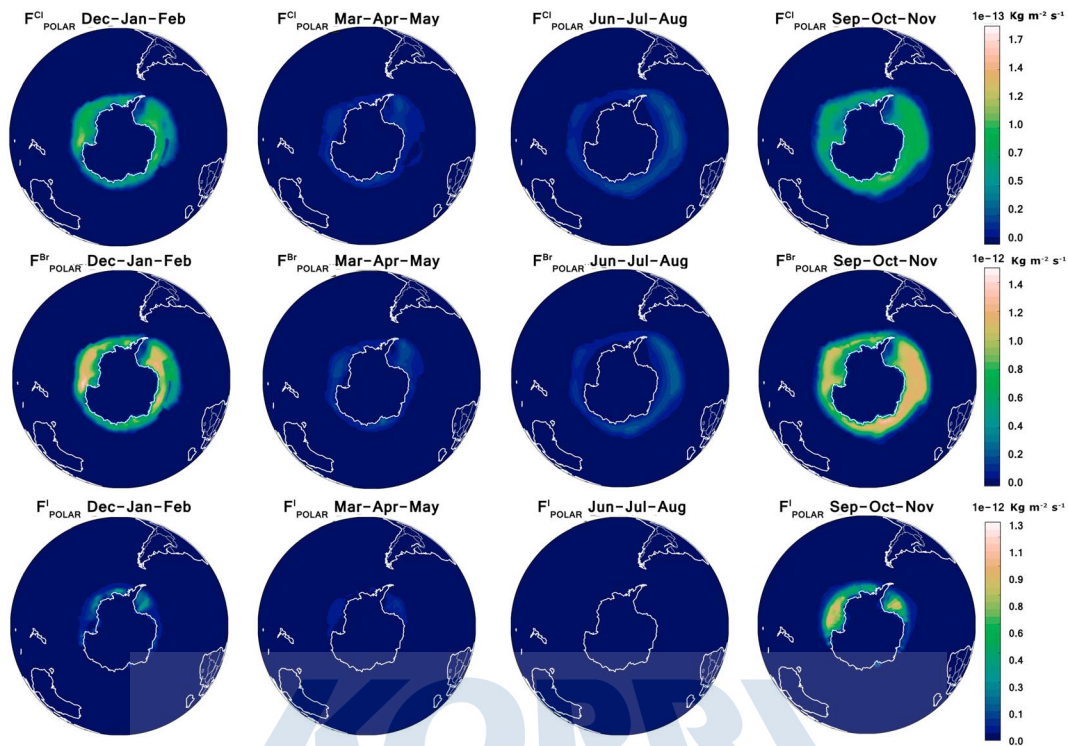
Figure 5. Seasonal distribution of the total polar sea-ice flux ($F_{POLAR} = F_{ICE} + F_{HET}$) within Antarctica for (top) chlorine, (middle) bromine, and (bottom) iodine. The flux strength within each panel has been computed by adding the monthly emissions for the three months of each season. The independent contribution of F_{ICE} and F_{HET} are shown in the supporting information.
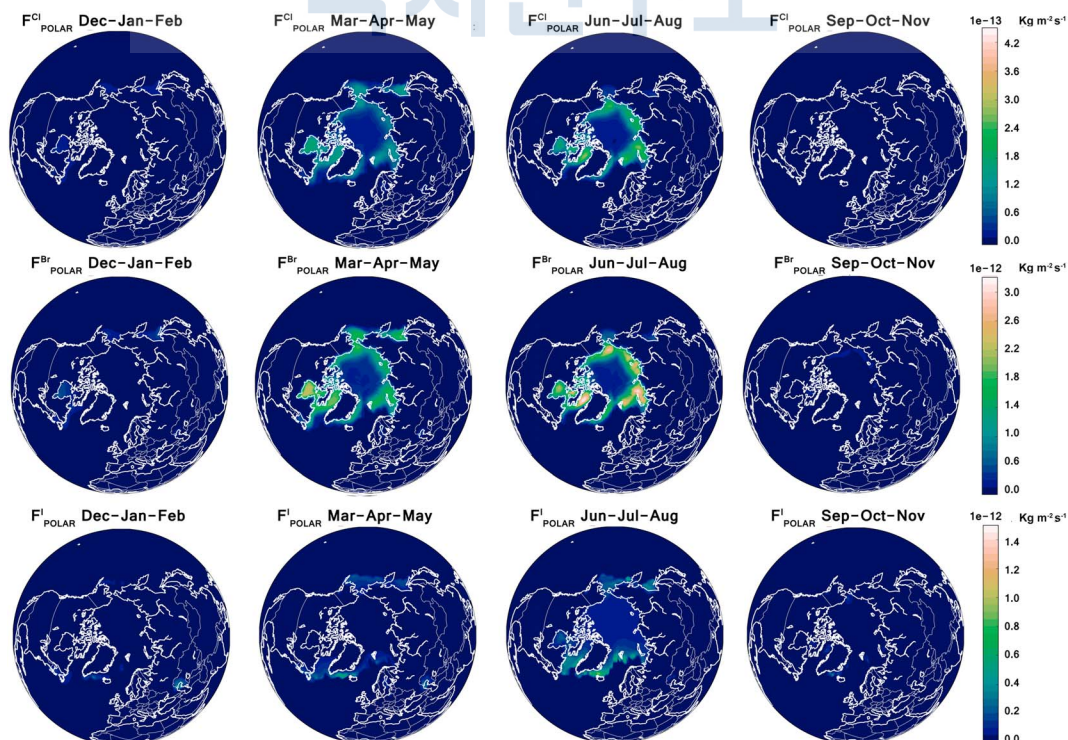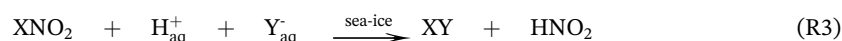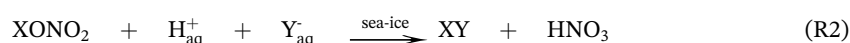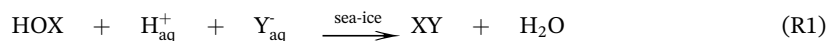

Figure 6. Same as Figure 5 but for the Arctic.

already been implemented in other investigations (e.g., Falk & Sinnhuber, 2018; Toyota et al., 2011; Yang et al., 2010). Briefly, this recycling begins with the initial deposition of a gas-phase oxidized halogenated molecule (in the form of HOX, $XONO_2$, and/or XNO_2) on ice and/or snow, which reacts and captures a reduced halide anion (Y^-_{aq}) to form a dihalogen molecule (XY), which escapes to the gas-phase due to its low solubility:

$$HOX \quad + \quad H^+_{aq} \quad + \quad Y^-_{aq} \quad \xrightarrow{\text{sea-ice}} \quad XY \quad + \quad H_2O \tag{R1}$$

$$XONO_2 \quad + \quad H^+_{aq} \quad + \quad Y^-_{aq} \quad \xrightarrow{\text{sea-ice}} \quad XY \quad + \quad HNO_3 \tag{R2}$$

$$XNO_2 \quad + \quad H^+_{aq} \quad + \quad Y^-_{aq} \quad \xrightarrow{\text{sea-ice}} \quad XY \quad + \quad HNO_2 \tag{R3}$$

The initial reduced halide species must exist in advance on the sea-ice surface to participate in the redox reaction. Even when the model considers an infinite halide reservoir at the sea-ice surface, the additional deposition of halogenated hydracids (HY) must account for the mass-balance required to refill the surface halide reservoir through:

$$HY \quad \xrightarrow{\text{sea-ice}} \quad H^+_{aq} \quad + \quad Y^-_{aq} \tag{R4}$$

Note that only a fraction of the deposited species can follow the redox reaction leading to reemission. Therefore, the initial deposition step also represents an efficient sink of halogens from the atmosphere into a large sea ice/snow pool that captures reservoir halogen species. In this way, the initial depositional flux can be interpreted as a repository that compensates for the assumption of an infinite halogen reservoir on the sea-ice.

The parameterized implementation of the heterogeneous recycling for bromine and chlorine follows:

$$F^{XY}_{HET}(i,t) = RE^{XY}_{N/S} \times \frac{\left(CF^{XONO2} \times D^{XONO2}_{FLX}(i,t) + CF^{XNO2} \times D^{XNO2}_{FLX}(i,t) + CF^{HOX} \times D^{HOX}_{FLX}(i,t)\right)}{CF^{XY}} \tag{3}$$

where (F^{XY}_{HET}) represents the surface XY emissions due to the heterogeneous recycling of halogen reservoirs deposited on sea-ice; $D^{XONO2}_{FLX}, D^{XNO2}_{FLX},$ and D^{HOX}_{FLX} represent the dry depositional flux of halogen nitrates, nitrites, and hypohalogenated acids, respectively, computed at the lower boundary for each model grid point and time of day; CF^{XONO2}, CF^{XNO2}, and CF^{HOX} are the conversion factors from mass flux (e.g., kg·m^{-2}·year^{-1}) to molecular flux (e.g., nmol·m^{-2}·day^{-1}) for each deposited species, and CF^{XY} is the equivalent inverse factor for converting nmol·m^{-2}·day^{-1} to kg·m^{-2}·year^{-1} (see Table 2). Finally, $RE^{XY}_{N/S}$ is the adjusted recycling efficiency for the release of each XY dihalogen species (i.e., analogous to a photochemical quantum yield indicating the probability that the reactive recycling follows each specific production channel). It is worth noting that equation (3) is only computed over sea ice-covered surfaces (e.g., following the logical condition $icefrac(i) > 0$), although the depositional terms (e.g., D^{XONO2}_{FLX}) remain active independently of the surface type (the deposition is allowed on all oceanic, icy, and continental surfaces). The recycling efficiency for each species, starting from their equivalent $RE^{XY}_{N/S}$ values used for sea-salt dehalogenation, is taken from previous CAM-Chem studies (Fernandez et al., 2014; Ordóñez et al., 2012; Saiz-Lopez et al., 2014) and adjusted considering the different sea-ice halide content prevailing in each hemisphere (Yang et al., 2010). As many interhalogen recycling reactions have been suggested to occur on the sea-ice surface and within the thin brine layer covering the Arctic and Antarctic frozen surfaces (Foster et al., 2001), equivalent expressions as those shown by reactions (R1) to (R4) can proceed forming both dihalogen and interhalogen products. Thus, a mixture of halogenated species, like IBr and BrCl, as well as I_2, Br_2, and Cl_2, are released back to the gas phase (see Table 2).

Note that the heterogeneous recycling flux (equation (3)) occurring on the first-year sea-ice does not explicitly consider the deposition of the reduced reservoir HX and does not impose any SZA dependence. This is justified considering that: (i) with a few exceptions, the HX deposition at the model surface largely surpasses that from $D^{XONO2}_{FLX} + D^{HOX}_{FLX}$; (ii) the sea-ice surface is already assumed to be an infinite halide reservoir, and thus the sea-ice halide content should not affect the kinetics of the process; and (iii) the diurnal variation (i.e., SZA dependence) of all inorganic halogen species is already considered in the gas-phase chemical

Table 2
Heterogeneous Recycling Emissions Implemented in the Polar Module

Heterogeneous recycling expression based on equations (3)[a] and (4)[b]	Adjusted parameters[c]
$F_{HET}^{Br2}(i,t) = RE_{N/S}^{XY} \times \dfrac{(CF^{BrONO2} \times D_{FLX}^{BrONO2}(i,t) + CF^{BrNO2} \times D_{FLX}^{BrNO2}(i,t) + CF^{HOBr} \times D_{FLX}^{HOBr}(i,t))}{CF^{Br2}}$	$RE_{N/S}^{XY} = 0.54 \quad ; \quad CF^{XY} = \dfrac{1.0 \times 10^{12} \times 86,400}{MW_{XY}}$
	$RE_{N/S}^{XY} = 0.3 \quad ; \quad CF^{XY} = \dfrac{1.0 \times 10^{12} \times 86,400}{MW_{XY}}$
$F_{het-rec}^{BrCl} = \begin{cases} RE_{N/S}^{XY}(Cl^-) \times \dfrac{(CF^{BrONO2} \times D_{FLX}^{BrONO2}(i,t) + CF^{BrNO2} \times D_{FLX}^{BrNO2}(i,t) + CF^{HOBr} \times D_{FLX}^{HOBr}(i,t))}{CF^{BrCl}} + \\ RE_{N/S}^{XY}(Br^-) \times \dfrac{(CF^{ClONO2} \times D_{FLX}^{ClONO2}(i,t) + CF^{ClNO2} \times D_{FLX}^{ClNO2}(i,t) + CF^{HOCl} \times D_{FLX}^{HOCl}(i,t))}{CF^{BrCl}} \end{cases}$	$\left.\begin{array}{l} RE_{N/S}^{XY}(Cl^-) = 0.36 \\ RE_{N/S}^{XY}(Br^-) = 0.30 \end{array}\right\} \; ; \; CF^{XY} = \dfrac{1.0 \times 10^{12} \times 86,400}{MW_{XY}}$
	$\left.\begin{array}{l} RE_{N/S}^{XY}(Cl^-) = 0.20 \\ RE_{N/S}^{XY}(Br^-) = 0.30 \end{array}\right\} \; ; \; CF^{XY} = \dfrac{1.0 \times 10^{12} \times 86,400}{MW_{XY}}$
$F_{HET}^{Cl2}(i,t) = RE_{N/S}^{XY} \times \dfrac{(CF^{ClONO2} \times D_{FLX}^{ClONO2}(i,t) + CF^{ClNO2} \times D_{FLX}^{ClNO2}(i,t) + CF^{HOCl} \times D_{FLX}^{HOCl}(i,t))}{CF^{Cl2}}$	$RE_{N/S}^{XY} = 0.1 \quad ; \quad CF^{XY} = \dfrac{1.0 \times 10^{12} \times 86,400}{MW_{XY}}$
	$RE_{N/S}^{XY} = 0.075 \quad ; \quad CF^{XY} = \dfrac{1.0 \times 10^{12} \times 86,400}{MW_{XY}}$
$F_{HET}^{I2}(i,t) = \dfrac{stq^I \times RE_{N/S}^{XY}}{CF^{I2}} \times \begin{pmatrix} CF^{IONO2} \times D_{FLX}^{IONO2}(i,t) + CF^{INO2} \times D_{FLX}^{INO2}(i,t) + CF^{HOI} \times D_{FLX}^{HOI}(i,t) \\ + CF^{IxOy} \times D_{FLX}^{IxOy}(i,t) + CF^{HI} \times D_{FLX}^{HI}(i,t) + CF^{SSA} \times D_{FLX}^{SSA}(i,t) \times r_{SSA}^I \end{pmatrix}$	$stq^I = 0.5 \; ; \; RE_{N/S}^{XY} = 0.7 \; ; \; CF^{XY} = \dfrac{1.0 \times 10^{12} \times 86,400}{MW_{XY}}$
	$stq^I = 0.5 \; ; \; RE_{N/S}^{XY} = 0.7 \; ; \; CF^{XY} = \dfrac{1.0 \times 10^{12} \times 86,400}{MW_{XY}}$
$F_{HET}^{IBr}(i,t) = \dfrac{stq^I \times RE_{N/S}^{XY}}{CF^{IBr}} \times \begin{pmatrix} CF^{IONO2} \times D_{FLX}^{IONO2}(i,t) + CF^{INO2} \times D_{FLX}^{INO2}(i,t) + CF^{HOI} \times D_{FLX}^{HOI}(i,t) \\ + CF^{IxOy} \times D_{FLX}^{IxOy}(i,t) + CF^{HI} \times D_{FLX}^{HI}(i,t) + CF^{SSA} \times D_{FLX}^{SSA}(i,t) \times r_{SSA}^I \end{pmatrix}$	$stq^I = 1.0 \; ; \; RE_{N/S}^{XY} = 0.3 \; ; \; CF^{XY} = \dfrac{1.0 \times 10^{12} \times 86,400}{MW_{XY}}$
	$stq^I = 1.0 \; ; \; RE_{N/S}^{XY} = 0.3 \; ; \; CF^{XY} = \dfrac{1.0 \times 10^{12} \times 86,400}{MW_{XY}}$

[a]The left column of the table presents the individual expressions for the induced recycling emission of each dihalogen species based on equation (3). D_{FLX}^{XONO2}, D_{FLX}^{XNO2}, and D^{HOX} represent the dry depositional flux of halogen nitrates, nitrites, and hypohalogenated acids computed at the lower boundary, respectively, for each model grid point and time of the day; CF^{XONO2}, CF^{XNO2}, and CF^{HOX} are the conversion factors from mass flux (e.g., $kg \cdot m^{-2} \cdot year^{-1}$) to molecular flux (e.g., $nmol \cdot m^{-2} \cdot day^{-1}$) for each deposited species, and CF^{XY} is the equivalent inverse factor for converting $nmol \cdot m^{-2} \cdot day^{-1}$ to $kg \cdot m^{-2} \cdot year^{-1}$; $RE_{N/S}^{XY}$ is the adjusted recycling efficiency for the release of each XY dihalogen source within each polar region. The expression is only computed whenever icefrac(i) > 0. [b]The F_{HET} expression for I_2 and IBr is based on equation (4) and is computed only when icefrac(i) > 0 and meltice(i) < 0.15. It includes the additional deposition of gas-phase HI and the high-order iodine oxides (IxOy = $2 \times I_2O_2 + 2 \times I_2O_3 + 2 \times I_2O_4$) as well as the surface depositional settling of sea-salt aerosols (D_{FLX}^{SSA}). $r_{SSA}^I = 7.27 \times 10^{-7}$ and represents the ratio of the iodide content of sea-salt aerosol respect to chloride, which is assumed to be equivalent to the seawater halide content ($[Cl^-_{aq}] = 0.53$ M and $[I^-_{aq}] = 3.9 \times 10^{-7}$ M). stq^I is a stoichiometric factor that assures that the recycling process occurring at the icy-surface does not capture an additional iodide ion from the infinite halogen pool. [c]The adjusted parameters for each expression in the left column are provided for the NH (top) and SH (bottom). The $RE_{N/S}^{XY}$ factor is dimensionless and represents relative fractions between 0 (zero) and 1 (one). $CF^{XY} = 1.0 \times 10^{12} \times 86,400 /MW_{XY}$; where MW_{XY} is the molecular weight for each bihalogen species in g/mol; and the following conversion factors are used: 86,400 s/day; 1×10^3 g/kg and 1×10^9 nmol/mol.

partitioning within our mechanism, which depends on the intensity of solar radiation at each model grid point. Quantitative evidence of these assumptions is provided in section 5.3, where a sensitivity analysis of the changes in the recycling efficiency when the F_{ICE} source is turned off is presented (i.e., considering the $VSL^{PM\text{-}ind}$ experiment).

For the case of iodine, several mechanisms have been proposed to release reactive halogen species to the polar atmosphere, such as the production of I_2 and tri-iodide (I_3^-) through the photo-oxidation of iodide (I^-_{aq}) in icy surfaces (Kim et al., 2016), and the heterogeneous photoreduction of iodate (IO_3^-) in ice, releasing an iodine-containing photofragment (Gálvez et al., 2016). Release of nitric oxide and I_2 from frozen iodide/nitrite solutions, including interhalogen chemical production through halide exchange, have also been suggested to occur on freezing sea-salt aerosol (O'Driscoll et al., 2006, 2008). Considering that these emission mechanisms are quite complex, we implement here a simplified "leapfrog" mechanism for polar iodine re-emission following a sequential series of deposition of iodine reservoirs, photo-induced heterogeneous recycling in ice (photo-oxidation of iodide and photoreduction of iodate) and re-emission of active gaseous iodine to the atmosphere, which initiates the process again. This is done by introducing a logical condition that allows the heterogeneous photochemical production of active iodine (Gálvez et al., 2016; Kim et al., 2016) following the deposition of iodine reservoir species over the snowpack/sea ice surface.

The "leapfrog"mechanism includes the additional contribution of sea-salt aerosol deposition at the sea-ice and snowpack surface, as described in equation (4):

$$F_{HET}^{I2}(i,t) = \frac{stq^I \times RE_{N/S}^{I2}}{CF^{I2}} \times \left(\begin{array}{c} CF^{IONO2} \times D_{FLX}^{IONO2}(i,t) + CF^{INO2} \times D_{FLX}^{INO2}(i,t) + CF^{HOI} \times D_{FLX}^{HOI}(i,t) \\ + CF^{IxOy} \times D_{FLX}^{IxOy}(i,t) + CF^{HI} \times D_{FLX}^{HI}(i,t) + CF^{SSA} \times D_{FLX}^{SSA}(i,t) \times r_{SSA}^I \end{array} \right)$$

(4)

where the first row in parenthesis is identical to equation (3) but for iodine species, and the second row includes the additional deposition of all iodine gas-phase reservoirs such as HI and the high-order iodine oxides ($I_xO_y = 2 \times I_2O_2 + 2 \times I_2O_3 + 2 \times I_2O_4$), as well as the surface deposition of sea-salt aerosols (D_{FLX}^{SSA}). The parameter r_{SSA}^I represents the iodine content of sea-salt aerosol, which is assumed to be equivalent to that in seawater (see Table 2). Note that the re-emission mechanism implemented for iodine differs from the one parameterized for bromine and chlorine in two main aspects: (i) for iodine, we include a stoichiometric photo-induced recycling factor (stq^I) to represent the heterogeneous recycling processes proposed in the literature (Gálvez et al., 2016; Kim et al., 2016); ii) following the proposed pH-dependent nitrite-induced reduction of iodate reservoirs occurring in frozen solutions, where the reduction efficiency is determined by the freeze concentration effect (Kim et al., 2019), we allowed the reactivation reaction to occur both at the sea-ice surface and also over the snowpack. This implementation of the iodine "leapfrog" mechanism allows the transport of iodine from coastal to the interior of Antarctica, thereby reproducing the satellite observations of IO over inner areas such as the Ronne and Ross ice-shelves (see section 4.2).

Note that the contribution of the heterogeneous recycling source (F_{HET}) has been added to the direct photochemical release (F_{ICE}) in Figures 5 and 6 ($F_{POLAR} = F_{ICE} + F_{HET}$) and that both contributions show equivalent strengths and distributions (see Figures S2 to S5 in the supporting information). This is expected since F_{HET} requires the prior existence of a gas-phase halogen species, which in the polar module is provided by F_{ICE}. As the geographical distributions of the individual species within each halogen family released to the atmosphere are very similar (for example, sources of Br_2, BrCl, and IBr show equivalent spatial patterns), the total halogen release for each halogen family (e.g., Cl, Br, and I) has been obtained by adding together the recycling contribution from each individual process shown in Table 2. The percentage contribution of each independent channel is provided in the supporting information.

3.4. Photochemical NO$_x$ Production From the Sea-Ice Surface

In-snow nitrate and nitrite photolysis occurring on the sea-ice surface has been demonstrated at several Arctic and Antarctic sites (Bauguitte et al., 2012; Domine et al., 2008; Jones et al., 2011), and represents an important source of nitrogen oxides to the polar troposphere, which influence ozone levels (Bloss et al., 2010). Here, based on Saiz-Lopez et al. (2008) and Boxe and Saiz-Lopez (2008), we introduced a SZA-dependent nitrogen dioxide surface flux (F_{ICE}^{NO2}) from the surface of multiyear sea-ice and snowpack following:

$$F_{ICE}^{NO2}(i,t) = F_0 \times H_{N/S} \times \frac{\cos(SZA(i,t))}{max_{SZA}}$$

(5)

where $\cos(SZA(i,t))$, max_{SZA}, and $H_{N/S}$ are equivalent variables to those defined in section 3.2. The initial NO$_2$ flux strength (F_0) has been adjusted iteratively starting from the initial value provided by Saiz-Lopez et al. (2008) for Antarctic summer conditions ($F_0 = 2.0 \times 10^8$ molec·cm^{-2}·s^{-1}), and the final values for all parameters are provided in Table S3 in the supporting information. Figure S6 shows the seasonal dependent spatial distribution of the sea-ice NO$_2$ source.

4. Model Validation and Performance: Distribution of Atmospheric Halogens in the Polar Regions

This section presents the validation of the performance of CAM-Chem at reproducing the ambient levels of halogen species in both polar regions when the online polar module is turned on. In doing so, note that the current model configuration (e.g., based on climatological sea-ice conditions and free running meteorology) was not intended to reproduce a particular set of observations from a specific campaign, but instead to
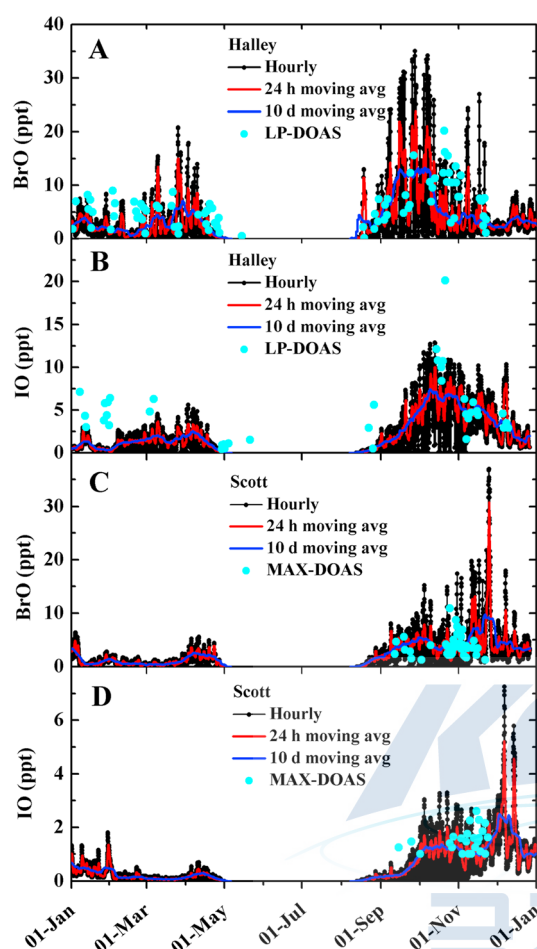
Figure 7. Annual variation of surface halogen oxides modeled at different Antarctic stations: (a) BrO Halley; (b) IO Halley; (c) BrO Scott; (d) IO Scott. The hourly concentrations, 24-hr moving averages and 10-day moving averages of modeled XO are indicated by a black dot line, red solid line, and blue solid line, respectively. Observations at each Antarctic base are superimposed with colored circles.

represent the major changes on the background polar halogen abundance when the sea-ice sources are considered.

Section 4.1 focuses on the measurement-model intercomparison of BrO and IO surface volume mixing ratios in Antarctica and the Arctic, as these are the reactive halogenated species most usually targeted. Additional validation for ClO is also presented for the Arctic. Besides the qualitative seasonal comparison between experimental and modeled time series, a standard statistical analysis is applied to determine the overall agreement throughout the period of time when each campaign took place. Simulated total BrO and IO columns within the polar regions are also compared against satellite retrieved BrO and IO columns in section 4.2. As the model simulation is based on climatological sea-ice extent, the satellite data have been averaged for 5–8 years (see section 2.2). This allows the analysis to focus on the mean geographical distribution of halogen oxides within the SH and NH. All the model-measurement evaluations presented in the main text have been performed considering the full polar setup (VSL^{PM-on}). To highlight the large changes in the modeled halogen representations when the polar module is turned on, equivalent comparisons considering the VSL^{PM-off} setup are provided in the supporting information.

4.1. Comparison With Surface Observations

Figures 7 and 8 show the annual variation of modeled and measured BrO and IO surface mixing ratios performed at the different Antarctic and Arctic measurements locations compiled in Table S1 of the supporting information. Modeled hourly values have been extracted at the closest model grid point with respect to the exact location of each station, and the CAM-Chem output at the surface has been multiplied by the THAMO scaling factor to account for the model variability in the BrO/IO vertical profile within the polar MBL (see section 2.3 and Table S2). A 24-hr (red) and a 10-day (blue) moving average have been applied to the daytime hourly model output. Equivalent results for the VSL^{PM-off} simulations are shown in Figures S7 and S8.

We begin the validation of surface values considering measurements performed at Halley station (Antarctica) for BrO and IO (Saiz-Lopez et al., 2007), as those are the only experimental data sets existent in polar regions covering a full annual cycle. Both modeled and experimental data show a marked seasonal cycle, with null values during austral winter and maximum halogen oxide mixing ratios during spring, which rapidly decrease during the summer (Figure 7). Maximum hourly modeled springtime values reach ~35 ppt for BrO and ~13 ppt for IO, with respective daily mean maxima of ~20 ppt and ~10 ppt which are maintained during September and October. This is in agreement with the reported BrO and IO peak values of 22 and 21 ppt, respectively, as well as with the observed seasonal cycle showing a secondary maximum during austral fall (Saiz-Lopez et al., 2007). This secondary maximum is related to the rapid increase in (i) the first-year sea-ice during March and April, which enhances the surface sea-ice flux before the beginning of the austral polar night; and (ii) the relative increase in the contribution of SSA dehalogenation source during fall in the SH (see section 5.1). The year-round surface BrO mean levels at Halley reach 5.9 and 5.0 ppt for the observations and model data, respectively, with a mean bias of −0.9 ppt that is smaller than the standard deviation (3.6 and 5.2 ppt, respectively, see Table 3). The maximum IO levels observed during October are well captured by the model. In comparison to BrO, the modeled seasonal IO peak is shifted to early spring due to the occurrence of phytoplankton blooms, which increase the F_{ICE}^{I2} flux within the Weddell Sea. During late summer and early fall, the model shows a continuous plateau of ~2 ppt of mean daily IO levels until null values are reached during the austral winter. Nevertheless, the overall hourly and daily modeled results show a reasonable agreement with respect to the measured IO variability and
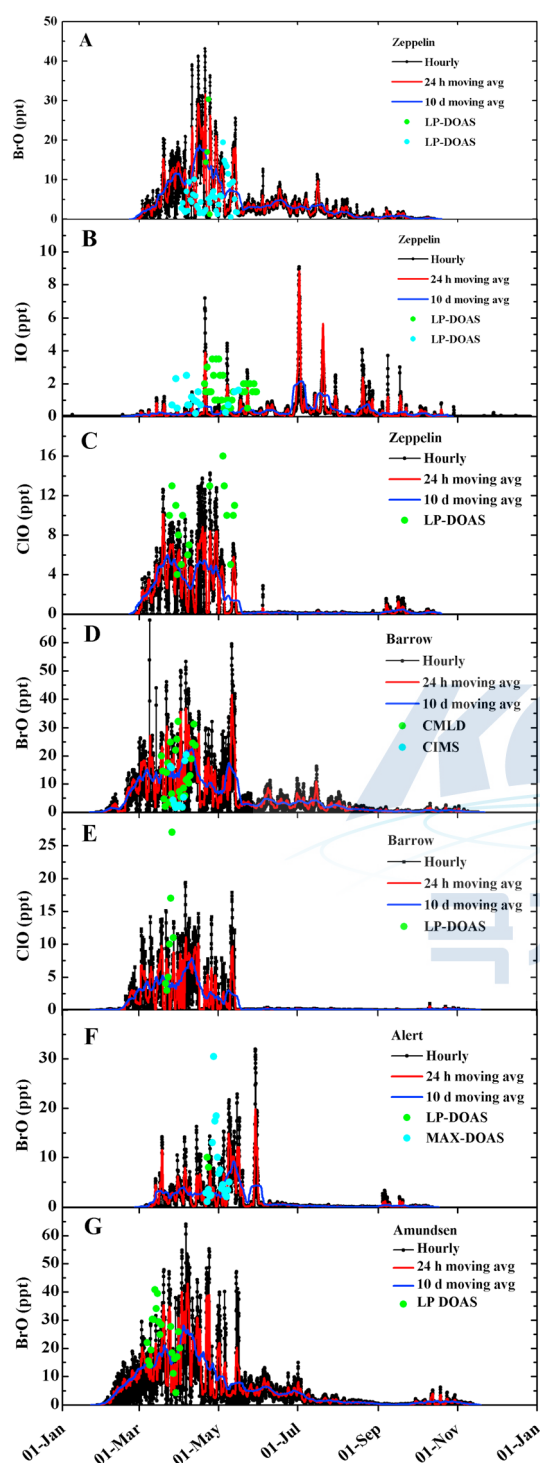
Figure 8. Same as Figure 7 but for Arctic stations: (a) BrO Zeppelin; (b) IO Zeppelin; (c) ClO Zeppelin; (d) BrO Barrow; (e) ClO Barrow; (f) BrO Alert; and (g) BrO Amundsen Gulf.

statistics (observed and modeled mean IO reaches 5.0 and 3.2 ppt, with a normalized mean bias (NMB) of −0.4, see Table 3). Note that the secondary maximum of IO is much less pronounced than that of BrO. This highlights that the initial sea-ice sources of bromine and iodine respond to different mechanisms.

For the case of the MAX-DOAS measurements performed at Scott base (Hay, 2011), the modeled BrO and IO values lie within their respective measurements range, showing a similar tendency and a small overestimation (mean bias of 4.1 and −0.1 ppt, respectively). Note, however, that the observed and modeled maximum IO values at Scott base appear during the end of the austral spring (Figure 7). For the case of BrO, a secondary maximum during the fall is also predicted by the model at Scott, although in this case there are no measurements to compare. Modeled IO results in summertime values that are larger than those observed during early spring, with a smooth decrease starting at the end of the summer and early fall.

Figure 8 shows the temporal evolution of modeled ClO, BrO, and IO surface mixing ratios and its comparison with Arctic measurements. Daily mean BrO surface mixing ratios measured during boreal spring are qualitatively well reproduced, although there is an apparent overestimation on the maximum values at Zeppelin and Barrow throughout the complete time series (Brooks et al., 2006; Liao et al., 2012). Note that to statistically compare the observed values with the model output (Table 3) we only extracted the model BrO peak for the same Julian day when measurements were performed, and computed a 6-hr model mean centered at the local time of the BrO peak. Table 3 shows $BrO^{max}_{obs} \approx 30$ ppt and $BrO^{max}_{mod} \approx 40$ ppt at Zeppelin, while the corresponding observed and modeled maximum values for Barrow are 32 and 47 ppt, determining an overall positive bias (NMB reaches 1.5 and 0.7 for each respective campaign). For the case of Alert and Amundsen, the model shows a small negative bias (NMB is −0.2 and −0.1, respectively), with maximum predicted values that are smaller than observations (Table 3). In general, modeled and measured standard deviations (st dev) largely surpass the absolute bias, indicating that the modeled and measured values used for validation are more spread than the mean difference between model and measurements. Note that the normalized mean error (NME) for Antarctic stations is usually smaller than that for the Arctic.

In contrast to BrO, modeled IO peaks at Zeppelin are continuously observed throughout the boreal spring, summer, and fall, which can be explained considering that the dominant iodine source around that location arises from the ocean surface (F_{OCN}) and not from the sea-ice. Indeed, the modeled IO surface levels follow the geographical distribution of the F^I_{OCN} source (see Figure S9 in the supporting information), and thus present maximum Arctic values at low latitudes. Note that the overall NMB = −0.6 indicates that the model underestimates the total polar iodine loading at that particular station. The model also predicts maximum ClO surface mixing ratios during boreal spring, consistent with BrO, of equivalent magnitude to those observed at Barrow and Zeppelin stations. Finally, it is worth highlighting that when the polar module is turned-off (e.g., for the $VSL^{PM\text{-off}}$ case), the modeled halogen oxides levels over the Arctic and Antarctica are at least 10 times smaller than the observations (Figures S7 and S8), highlighting the importance of considering sea-ice sources in the polar regions.

Table 3
Statistical Analysis of CAM-Chem Performance in Reproducing Surface BrO and IO Observations in the Arctic and Antarctica

Station	Species	Observed[a] Mean	Max	St dev	Model[a] Mean	Max	St dev	Mod-Obs[b] Bias	NMB	NME
Zeppelin	BrO	6.6	30.3	5.9	16.4	40.2	10.4	9.9	1.5	2.0
Zeppelin	IO	1.5	3.5	0.8	0.6	4.9	1.1	−0.8	−0.6	0.9
Zeppelin	ClO	9.5	16.0	3.5	5.1	13.5	3.6	−4.3	−0.5	0.5
Barrow	BrO	11.8	32.1	9.1	20.3	47.0	13.5	8.5	0.7	1.1
Barrow	ClO	11.0	27.0	8.6	6.9	12.4	4.3	−4.1	−0.4	0.8
Alert	BrO	8.3	30.5	7.0	6.8	20.3	5.4	−1.5	−0.2	1.0
Amundsen	BrO	23.5	40.9	9.4	20.8	38.4	10.3	−2.7	−0.1	0.5
Halley	BrO	5.9	20.2	3.6	5.0	27.8	5.2	−0.9	−0.2	0.7
Halley	IO	5.0	20.1	3.9	3.2	9.3	3.1	−1.9	−0.4	0.6
Scott	BrO	3.8	10.9	2.0	7.9	21.7	5.4	4.1	1.1	1.3
Scott	IO	1.5	2.6	0.5	1.4	2.2	0.5	−0.1	−0.1	0.3

Note. The statistical analysis has been performed by selecting the closest model grid point to the exact location of each polar base and extracting the BrO, ClO, and IO daily peak from the model for the same Julian day when measurements were performed. The mean value is computed considering a 6-hr range centered at the local time of the daily peak.
[a]Units for observed and modeled mean, maximum (max), and standard deviation (st dev) are parts per trillion by volume (ppt). [b]Units for the model-observation (Mod-Obs) bias are also ppt, while the normalized mean bias (NMB) and normalized mean error (NME) are dimensionless.

4.2. Comparison With Satellite VCDs

In order to validate the halogen oxide geographical distributions obtained with CAM-Chem, we have computed the monthly mean vertical columns for BrO and IO (i.e., the vertical column density at each model grid point) and compared these to BrO columns retrieved from GOME-2A (Blechschmidt et al., 2016) and IO columns from SCIAMACHY (Schönhardt et al., 2012), respectively. As the original satellite data have a much finer spatial resolution than the global model (e.g., the original pixel size of the GOME-2 data is 40×80 km^2 and for SCIAMACHY data is $0.25° \times 0.25°$), we initially averaged the satellite data onto a $0.5° \times 0.5°$ grid considering all observation times and orbits within each month, and further computed the monthly mean for the years 2007–2011 (GOME-2A) and 2004–2011 (SCIAMACHY). In a second step, the satellite data were regridded onto the $1.9° \times 2.5°$ resolution in CAM-Chem. To ensure a proper timing during the model/satellite comparison, CAM-Chem output was extracted between 9:00 and 11:00 local time at all model grid points. This covers the range of satellite observation times over the polar regions (section 2.2).

The modeled spatial distribution of BrO total VCDs presents a reasonable agreement with the geometric VCD GOME-2A retrievals (Figure 9), presenting maximum values during boreal Arctic spring that decrease in magnitude toward the summer. The simulated spatial distribution show large BrO VCDs areas located close to the geographical Arctic circle (i.e., 66°N) and maximize above first-year sea-ice regions in coincidence with the surface BrO plumes (see Figure S9), highlighting the contribution of lower troposphere BrO to the total vertical column. The spatial location of the BrO VCDs maxima observed from satellite is well reproduced for some areas, but the simulated distribution also differs from observations in other regions: for example, in April, the model captures the high values measured over the west of Greenland, while the measured peak values between the East Siberian and Beaufort sea are not reproduced by the model. Note, however, that the exact locations of the BrO VCD plumes are expected to differ between the model and the satellite observations, as the GOME-2A data have been averaged from 2007–2011 while the model is run in free-running mode, and thus, it is not representative of the meteorology of any specific year (see section 2.1). There is a model negative VCD bias throughout the year (ranging between -0.1×10^{13} and -2.5×10^{13} molec/cm^2), with larger differences appearing during the boreal summer months. This overall negative bias is partially reduced when *meltice* is considered in equation (1): for example, the relative contribution of *meltice* and *newice* to the surface sea-ice flux are of equivalent magnitude during May and June (Figure 4). As the magnitude and evolution of surface BrO is generally well reproduced in the model, the observed VCD differences most probably arise due to an underestimation of modeled free tropospheric BrO which, in turn, could imply that the SSA recycling process is not properly represented in the simulations and/or the model overestimates the washout efficiency of inorganic bromine in the free troposphere. It is less likely that the model/observation VCD difference arise from stratospheric BrO, as the CAM-Chem
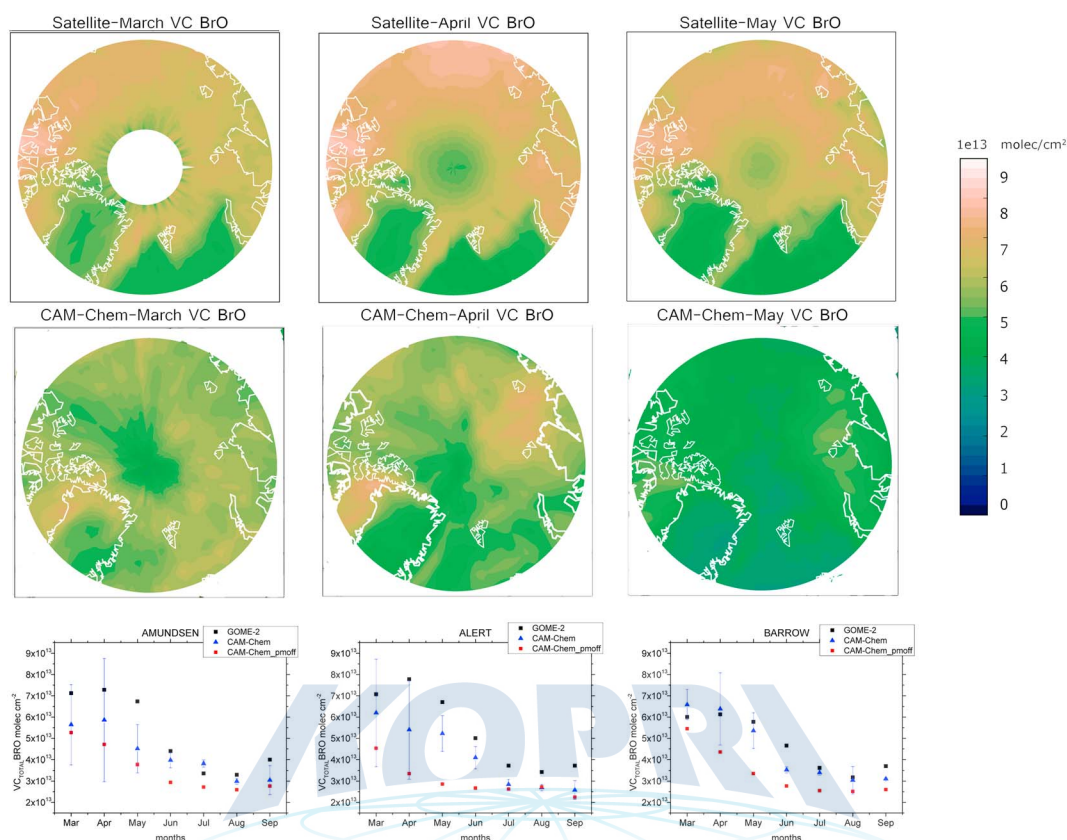
Figure 9. Springtime monthly mean climatology (averaged over 2007–2011) of BrO geometric VCDs from (top) GOME-2A and (middle) CAM-Chem for the Arctic. A latitudinal mask has been applied as satellite data is derived poleward of 70°N. (bottom) Seasonal variation of BrO VCDs above different Arctic stations. Error bars in the modeled values correspond to the standard deviation. GOME-2A = Global Ozone Monitoring Experiment-2A; CAM-Chem = Community Atmosphere Model with Chemistry.

climatological performance in the stratosphere has already been validated against WACCM and other high top global models (Fernandez et al., 2014, 2017; Tilmes et al., 2016). Additionally, note that the satellite retrieval is less sensitive over regions with low surface albedo so that retrieved geometric VCDs are expected to underestimate the tropospheric contribution to the total columns over the open ocean. Independently of the overall negative bias, it is worth highlighting the general capability of the model to reproduce the BrO VCD seasonality at all Arctic stations, as well as a consistent spatial distribution.

An equivalent general analysis of the model performance can be made for Antarctica. The seasonal variation and spatial distribution of BrO VCDs above Antarctica show a much better agreement to the satellite retrievals during early austral spring, presenting a small underestimation during late spring and summer (Figure 10). The model predicts maximum BrO VCDs located above 1st-year sea-ice covered areas, following the spatial patterns of the total sea-ice flux observed in Figure 5. The mean bias of the BrO VCD for Antarctica is smaller than that observed for the Arctic (ranges between -0.1×10^{13} and -1.5×10^{13} molec/cm^2), with the larger differences above the Antarctic snowpack and around the Southern Ocean (i.e., within the 50–60°S latitudinal band). The latter is a region characterized by persistent and strong winds that produce large amounts of sea-salt aerosols, leading to enhanced SSA dehalogenation in the free troposphere, which in turn, affects the BrO abundance above the MBL (section 5.1). Indeed, the difference between the GOME-2A data and CAM-Chem for the BrO vertical column above the Southern Ocean peaks during the summer months, suggesting that a considerable portion of the bias between satellite and model results could arise from the free troposphere.

We now evaluate the model performance for IO column densities observed above Antarctica (Figure 11). Note that the satellite IO VCD is computed as a differential column with respect to the reference in the remote Pacific (i.e., within the 30–50°S and 150–170°W region, see section 2.2), assuming a zero IO
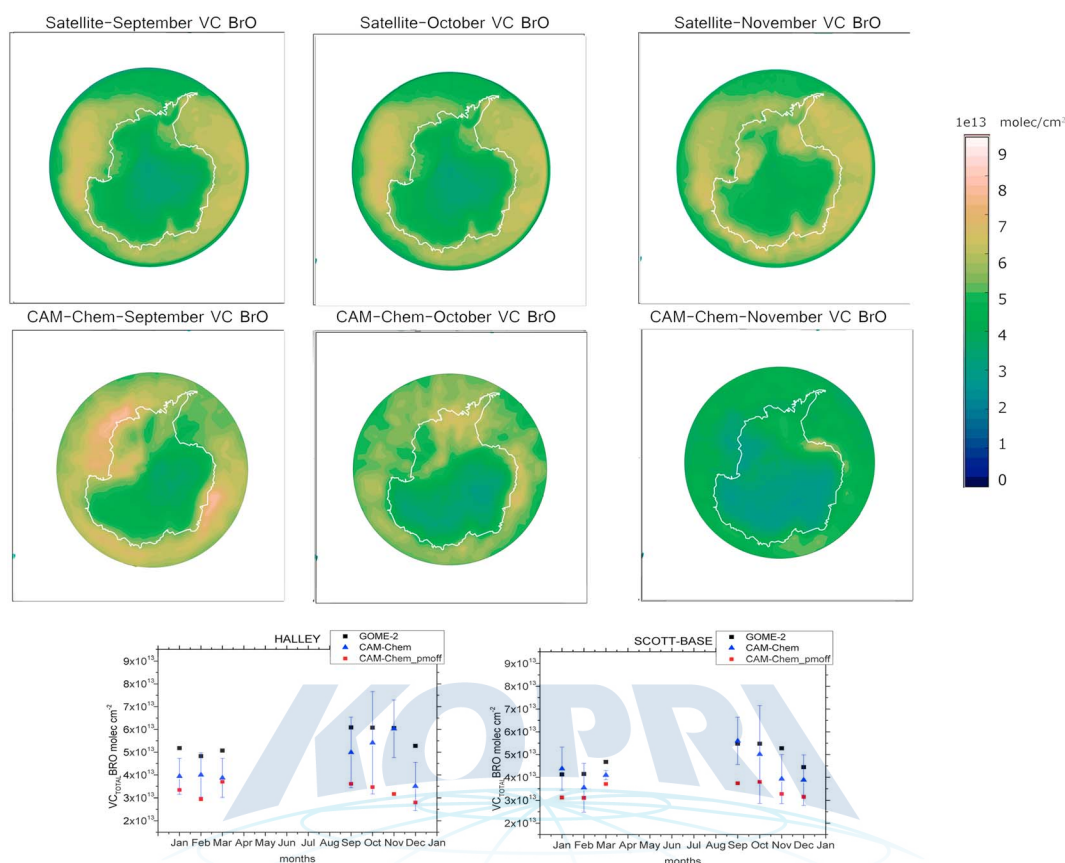
Figure 10. Same as Figure 9 but for Antarctica. The latitudinal mask has been applied poleward of 60°S.

reference. The CAM-Chem IO VCD within that reference area reaches a mean annual value of 5.6×10^{11} molec/cm^2, which can represent in cases half of the total IO VCD retrieved by the satellite above the sea-ice covered areas. Thus, in order to quantitatively compare the IO VCD results, we subtracted the modeled monthly IO VCD mean within the remote Pacific reference area from the CAM-Chem VCD output (hereinafter referred to "CAM-Chem corrected" output, Table 4). Overall, the implementation of the polar module allows the model to achieve a satisfactory Antarctic IO VCD whose maximum and background levels are in reasonable agreement with those retrieved from SCIAMACHY, including several areas (such as the Weddell and Ross seas) and times (October and November) with overlapping enhancements in tropospheric IO. The implementation of the iodine "leapfrog" mechanism described in section 3.3 results in the propagation of active iodine from coastal to inner regions of Antarctica, reproducing satellite IO measurements over the interior of the continent. It is worth to mention that the observed IO enhancements are in general fairly close to the detection limit and that the satellite spatial distribution is influenced by the varying albedo above the sea-ice and snowpack, which is assumed to be constant during the retrieval. Additionally, the shielding due to clouds (and on a smaller scale atmospheric aerosols or blowing snow) might be relevant because the satellite would see less IO above those areas, and the retrieval algorithm does not include any cloud filter. Further measurements performed by new satellite instruments with improved signal-to-noise ratio and spatial resolution may help to perform more accurate comparisons in the future. The model captures quite well the observed seasonal trends for both stations, presenting a small underestimation at Halley and a slight overestimation at Scott during September.

5. Quantification of Halogen Emissions From the Polar Regions

This section quantifies the sea-ice halogen emissions and compares them to the ocean VSL halocarbon fluxes already implemented in the benchmark CAM-Chem setup within each polar cap (defined as poleward of 50°
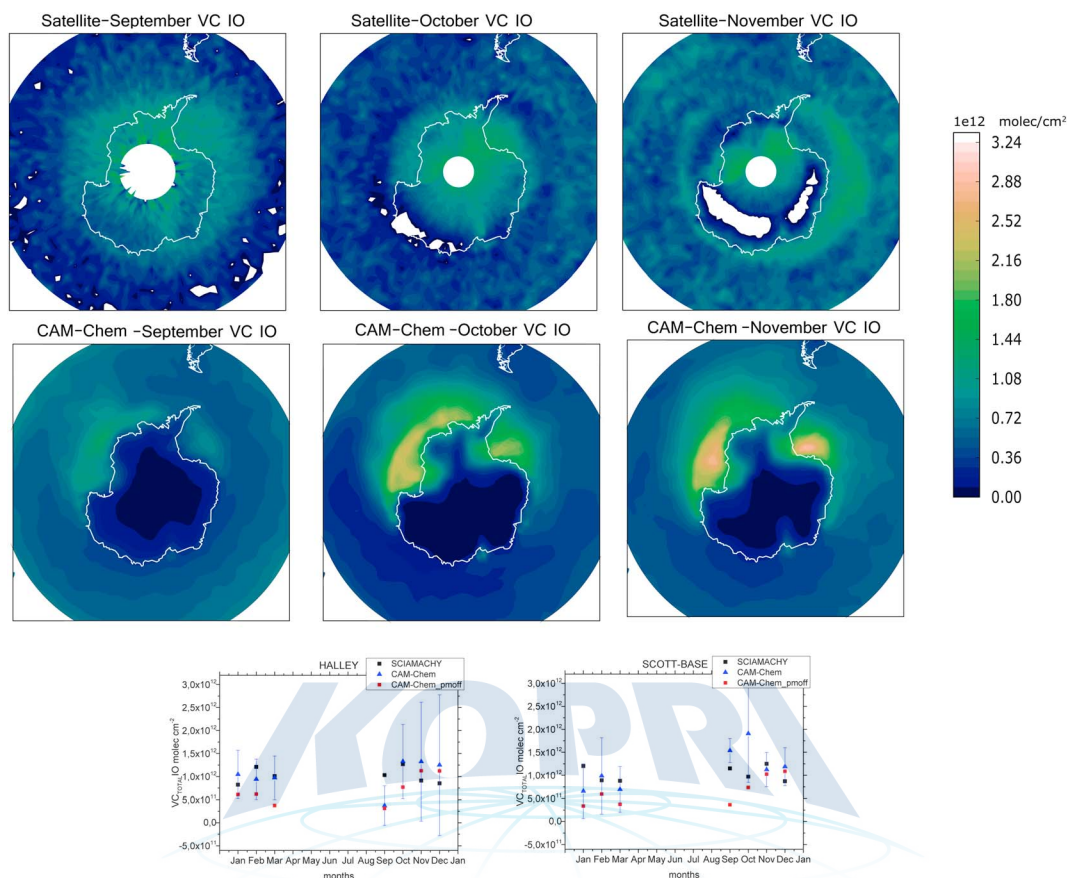
Figure 11. Springtime monthly mean distribution (averaged from 2004 to 2011) of total IO VCDs retrieved from (top) SCIAMACHY and (middle) CAM-Chem for the SH. All data are shown poleward from 50°S. CAM-Chem output has been corrected by subtracting the modeled reference IO VCDs from the remote Pacific (30–50°S and 150–170°W). (bottom) Seasonal variation of IO VCDs above different Antarctic stations. Error bars in the modeled values correspond to the standard deviation. SCIAMACHY = SCanning Imaging Absorption SpectroMeter for Atmospheric CHartographY; CAM-Chem = Community Atmosphere Model with Chemistry.

latitude in each hemisphere). We have also conducted sensitivity runs to estimate the uncertainty in the sea-ice emission flux by iteratively modifying the flux from our best-adjusted value until the bias shows a persistent disagreement with observations. We estimate an uncertainty of ±50% in the computed halogen

Table 4
Statistical Analysis of the CAM-Chem Performance in Reproducing BrO (GOME-2A) and IO (SCIAMACHY) VCDs Above Different Arctic and Antarctic Stations

Station	Species	Observed[a]			Model[a]			Mod-Obs[b]		
		Mean	Max	St dev	Mean	Max	St dev	Bias	NMB	NME
Barrow	BrO	5.2	7.5	1.8	4.5	6.6	1.6	−0.7	−0.2	0.2
Alert	BrO	5.3	8.1	1.8	4.2	6.7	1.8	−1.1	−0.3	0.3
Amundsen	BrO	4.6	6.9	1.6	4.3	5.9	1.1	−0.4	−0.1	0.2
Halley	BrO	5.5	6.1	0.5	4.3	6.2	1.0	−1.2	−0.3	0.3
Halley	IO[c]	1.0	1.3	0.2	1.1	1.4	0.5	0.1	0.05	0.4
Scott	BrO	4.8	5.5	0.6	3.8	6.3	1.8	−0.5	−0.1	0.2
Scott	IO[c]	1.0	1.3	0.2	1.1	2.0	0.6	0.1	0.1	0.4

[a]Values for observed and modeled mean, maximum (max), and standard deviation (st dev) have been divided by 10^{13} molec/cm^2 for the case of BrO VCDs and by 10^{12} molec/cm^2 for the case of IO VCDs. The model st dev was computed considering the 9:00–11:00 mean value for each day at the closest grid point to each polar base. The satellite st dev considers the monthly variation of all satellite pixels within each model grid point. [b]The model-observation (Mod-Obs) bias has also been divided by 10^{13} molec/cm^2 for BrO and by 10^{12} molec/cm^2 for IO, while the normalized mean bias (NMB) and normalized mean error (NME) are dimensionless. [c]For the case of IO VCDs, "CAM-Chem corrected" values (i.e., subtracting the monthly IO VCD mean within the remote Pacific reference area from the modeled CAM-Chem VCD output) have been used. See text for details.

Table 5
Halogen Annual Emission Flux Arising From Each of the Independent Sources Implemented in the Polar Module

Region	Antarctica			Arctic		
Species[a]	Chlorine	Bromine	Iodine	Chlorine	Bromine	Iodine
F_{ICE}	19.6	160.2	19.4	17.5	167.4	3.0E−2
F_{HET}	12.3	89.7	19.4	15.0	103.2	3.8
F_{POLAR}	**31.9**	**249.9**	**38.8**	**32.5**	**270.6**	**3.9**
F_{OCN}^{I}	0.0	0.0	4.0	0.0	0.0	27.0
F_{VSL}^{srf}	0.2	0.6	3.1	0.4	1.0	4.6
F_{SSA}^{srf}	9.0	20.7	0.0	8.6	21.4	0.0
F_{SRF}	**41.2**	**271.1**	**45.9**	**41.5**	**292.9**	**35.5**
F_{VSL}^{trop}	2.7	21.3	32.7	5.0	27.0	32.6
F_{SSA}^{trop}	85.6	146.8	0.0	68.0	109.0	0.0
F_{TROP}	**120.3**	**417.9**	**75.5**	**105.4**	**406.6**	**63.5**

[a]All values correspond to the $VSL^{PM\text{-}on}$ experiment and are given in Gg X year^{-1}, where X stands for Cl, Br, and/or I. F_{ICE} represents the photochemical sea-ice emissions (section 5.2), F_{HET} represents the heterogeneous recycling emission (section 5.3), and $F_{POLAR} = F_{ICE} + F_{HET}$. F_{OCN}^{I} is the total oceanic iodine flux (section 5.1). For the case of the VSL halogen photochemical release (F_{VSL}) and the SSA dehalogenation source (F_{SSA}), the mean annual flux has been computed, differentiating the emission occurring at the surface (F_{VSL}^{srf} and F_{SSA}^{srf}) from that occurring throughout the whole troposphere (F_{VSL}^{trop} and F_{SSA}^{trop}). F_{SRF} adds up all of the original sources implemented in the VSL halogen version of CAM-Chem plus the sources arising from the surface of each polar cap ($F_{SRF} = F_{POLAR} + F_{OCN}^{I} + F_{VSL}^{srf} + F_{SSA}^{srf}$). F_{TROP} quantifies the overall atomic halogen flux integrated within the whole troposphere for each polar cap ($F_{TROP} = F_{POLAR} + F_{OCN}^{I} + F_{VSL}^{torp} + F_{SSA}^{trop}$). Note that each bold row shows the sum of the flux strength of the preceding non-bold rows plus F_{POLAR}.

emission flux. Beyond this uncertainty range, the model either clearly underestimates or overestimates the observations. To help with readability, we ordered the text so that results in sections 5.1 to 5.4 correspond to processes described in sections 3.1 to 3.4, respectively. Finally, section 5.5 compares the contribution of each independent source and provides individual mean results for different seasons. All the annual flux estimations presented here have been performed for the $VSL^{PM\text{-}on}$ experiment unless stated otherwise.

5.1. Oceanic and SSA Emissions of Halocarbons and Inorganic Halogens

Table 5 presents the total annual release of halogen atoms from VSL photodecomposition (i.e., considering both hν + OH reactivity) for chlorine, bromine, and iodine, separated for the Northern and Southern polar caps. As VSL halocarbon photodecomposition in the atmosphere does not occur instantaneously but depends on the effective chemical lifetime of each species, we separately integrated the X atom production rate from VSL degradation occurring only at the lowest level of the model (F_{VSL}^{srf}, which is representative of the photochemical breakdown in the MBL) with respect to the total halogen release integrated in the troposphere (F_{VSL}^{trop}). The VSL halogen emission flux for each family is very similar between both polar regions (F_{VSL}^{srf} = 0.2, 0.6, and 3.1 Gg/year for chlorine, bromine, and iodine in Antarctica, respectively, and 0.4, 1.0, and 4.6 Gg/year within the Arctic), which is expected to be the case as the Ordóñez et al. (2012) inventory considers equivalent emission strength for all halocarbons within northern and southern high latitudinal bands. We use F_{VSL}^{srf} to compare the contribution of VSL halocarbons respect to other sea-ice sources afecting to surface BrO and IO levels. F_{VSL}^{trop} is used in the comparison with BrO/IO columns.

Table 5 also shows the annual mean inorganic iodine source released by the ozone-mediated oxidation of seawater iodide at the ocean surface (F_{OCN}^{I}, in the form of HOI and I$_2$), which is computed online and released in the lowest layer of the model (see section 3.1). Note that for the SH polar cap, F_{VSL}^{srf} and F_{OCN}^{I} for iodine are of equivalent magnitude, while for the Arctic $F_{OCN}^{I} \approx 6 \times F_{VSL}^{srf}$. This responds to the larger anthropogenic ozone background in the NH high latitudes MBL: high ozone levels around Europe and North America enhance oceanic iodine emissions from the sea surface, which in turn regulate MBL ozone destruction through a negative feedback mechanism (Prados-Roman, Cuevas, Fernandez, et al., 2015).

The annual emission strength of the SSA dehalogenation process, separated into their surface (F_{SSA}^{srf}) and tropospheric (F_{SSA}^{trop}) contributions is also listed in Table 5. Several interesting features result from the

implementation of the SSA dehalogenation source. These are exemplified for the Southern Hemisphere: first, the vertically integrated SSA dehalogenation contribution is the largest source of chlorine throughout the polar troposphere (F_{SSA}^{trop} = 85.6 Gg Cl/year), surpassing the photochemical release from VSLs (F_{VSL}^{Cl} = 2.7 Gg Cl/year) as well as the chlorine source from the sea-ice surface (F_{ICE}^{CL2} + F_{ICE}^{BrCl} = 19.6 Gg Cl/year and F_{HET}^{XY} = 12.3 Gg Cl/year, see below); second, the surface sea-ice flux is the predominant source of bromine (F_{POLAR} = 249.9 Gg Br/year) and controls surface halogen chemistry over the Antarctic (F_{VSL}^{srf} = 0.6 Gg Br/year and F_{SSA}^{srf} = 20.7 Gg Br/year), although the overall aerosol contribution integrated in the tropospheric column (F_{SSA}^{trop} = 146.8 Gg Br/year) is of equivalent magnitude; third, there is a marked and rapid decrease in the SSA dehalogenation flux moving up in the troposphere as well as moving into continental Antarctica or out to the open ocean, which responds to the quite rapid washout lifetime of SSA in the model. Hence, the SSA source has a large impact on tropospheric halogens mainly above the open ocean areas (see section 4.2), but it does not represent a significant contribution to maintaining the large halogen burden required to reproduce the polar surface observations of BrO and IO presented in section 4.1. Note that for the case of iodine, SSA dehalogenation does not represent a net source but only constitutes an additional process changing the gas-phase partitioning (Saiz-Lopez et al., 2014).

5.2. Emissions From the Sea-Ice Surface: Photochemical and Biologically Induced Sources

The global annual flux of inorganic chlorine and bromine photochemically released from the sea-ice surface for the SH reaches 19.6 and 160.2 Gg/year, respectively, while in the NH it adds up to 17.5 and 167.4 Gg/year (Table 5). The slightly larger annual values for the NH result mainly from the larger *newice* area accumulated throughout the year, as well as the smaller max_{SZA} adjusted parameter for equation (1) within the Arctic. For the case of iodine, the annual mean emission of the biological source from underneath the sea-ice (F_{ICE}^{I2}) in the SH is approximately 5 times larger than the oceanic polar emission and ~6 times larger than the F_{VSL}^{srf} iodine source. In contrast, for the NH the sea-ice iodine emission is negligible ($F_{ICE}^{I2} \approx 3 \times 10^{-2}$ Gg/year). Therefore, ~75% of the total Arctic iodine comes from the ocean (F_{OCN}^{I}), while the remaining is provided by F_{VSL}^{srf}. The convergence of several emission drivers enhances the relative contribution of F_{ICE}^{I2} in Antarctica with respect to the Arctic, in what has been called the "polar iodine paradox" (Saiz-Lopez & Blaszczak-Boxe, 2016): larger first-year sea-ice coverage and thinner sea-ice thickness prevails in Antarctica, which enhances the photochemical biotic production of iodide underneath the sea-ice and favors the transport of I$_2$ through brine channels up to the sea-ice surface. On the other hand, the dominant thick and compact multiyear sea-ice prevailing in the Arctic, shields the microalgae colonies underneath the sea-ice from the weak solar radiation, reducing the iodide biological production and brine diffusion from below the sea-ice. This is represented in the polar module by a reduced efficiency (40 times smaller) in the "production + diffusion coefficient" for the NH ($H_{N/S}$ = 0.01) with respect to the SH ($H_{N/S}$ = 0.4) in equation (2).

5.3. Heterogeneous Recycling of Halide Reservoirs at the Sea-Ice Surface

The absolute annual recycling emission flux (F_{HET}) for each halogen species for the $VSL^{PM\text{-}on}$ experiment are also given in Table 5. Due to the larger Arctic ocean and sea-ice salinity (represented by a higher northern recycling efficiency ($RE_{N/S}^{XY}$) for all Arctic expressions in Table 2) as well as the larger sea-ice extent, F_{HET}^{Cl} and F_{HET}^{Br} contributions to the total polar source is greater in the Arctic than in Antarctica. An additional factor increasing the Arctic recycling efficiency with respect to the SH is the overall larger NO$_x$ background, which shifts the inorganic chlorine/bromine gas-phase partitioning to the formation of halogen nitrates and nitrites (e.g., ClONO$_2$, ClNO$_2$), thus increasing the deposition of oxidized species that initiates the heterogeneous recycling process. Note that the recycling emission for bromine and chlorine is smaller than the initial photochemical emission quantified in section 5.2: for example, in Antarctica F_{HET}^{Br} represents only 60% the sum of F_{ICE}^{Br2} + F_{ICE}^{BrCl}. For the case of Antarctic iodine, the sea-ice recycling includes the contribution of all inorganic reservoirs and sea-salt iodine, and as a consequence $F_{HET}^{I} \approx F_{ICE}^{I2}$. Indeed, the flux strength is modeled to be smaller in the Arctic (F_{HET}^{I} = 3.8 Gg I/year) than in Antarctica (F_{HET}^{I} = 19.4 Gg I/year) due to the different locations of the initial surface flux releasing gas-phase iodine: while in the Arctic the dominant source is the ocean which shows enhanced strength at low latitudes further away from the ice-covered regions, in Antarctica the initial flux results directly from the plankton colonies underneath and within sea-ice. In general, the seasonal variation of F_{HET} follows the shape of the sea-ice source (F_{ICE}).

Table 6
Depositional Flux of Each Halogen Species for the Different Experiments

| Species | Antarctica | | | | | | Arctic | | | | | |
| | Chlorine | | Bromine | | Iodine | | Chlorine | | Bromine | | Iodine | |
Experiment	$VSL^{PM\text{-}on}$	$VSL^{PM\text{-}ind}$	$VSL^{PM\text{-}on}$	$VSL^{PM\text{-}ind}$	$VSL^{PM\text{-}on}$	$VSL^{PM\text{-}ind}$	$VSL^{PM\text{-}on}$	$VSL^{PM\text{-}ind}$	$VSL^{PM\text{-}on}$	$VSL^{PM\text{-}ind}$	$VSL^{PM\text{-}on}$	$VSL^{PM\text{-}ind}$
D_{FLX}^{ox} (Gg X year^{-1})[a]	4.6	4.7	58.7	14.4	15.8	2.1	5.9	3.1	68.8	9.8	3.7	3.9
D_{FLX}^{red} (Gg X year^{-1})[a]	28.5	12.0	128.8	19.0	0.4	0.1	25.8	7.5	124.0	8.2	0.1	0.1
F_{HET} (Gg X year^{-1})[a]	12.3	5.4	89.7	23.2	19.4	1.7	15.0	3.6	103.2	16.7	3.8	4.0

[a]The depositional fluxes of oxidized (D_{FLX}^{ox}) and reduced (D_{FLX}^{red}) reservoir species, as well as the heterogeneous recycling flux (F_{HET}), are given in Gg X year^{-1}, where X stands for Cl, Br, and/or I.

Besides the $XONO_2$ and HOX depositional flux (D_{FLX}^{ox}), it is worth noting that the HY deposition (D_{FLX}^{red}) also contribute to increase the halide content available at the sea-ice and snowpack surfaces, although many complex geochemical factors affect the surface halide concentration (Abbatt et al., 2012). Thus, D_{FLX}^{red} does not always account for the halogen mass-balance required to refill the halide uptake occurring at the sea-ice surface. Table 6 shows that for bromine and chlorine $D_{FLX}^{red} > D_{FLX}^{ox}$ both in the Arctic and Antarctica. This justifies the assumption that D_{FLX}^{ox} controls the maximum possible halogen contribution arising from the heterogeneous recycling processes. But for the case of chlorine, the deposition of oxidized chlorine species in the Arctic (D_{FLX}^{ox} = 5.9 Gg Cl/year) is not enough to provide the total chlorine mass (in the form of Cl_2) to compensate for the heterogeneous recycling flux (F_{HET}^{Cl} = 15.0 Gg Cl/year). This is partially compensated by a larger contribution of BrCl emission to the total chlorine flux, which results from the release of a chloride ion by the recycling of an oxidized bromine reservoir (mainly $BrONO_2$) whose depositional flux to the surface largely surpass that of oxidized chlorine reservoirs. This is not the case for iodine, which presents a marked imbalance in the surface deposition of reduced species (i.e., HI), that represents at most 5% of the heterogeneous recycling flux required to account for the total iodine emission (D_{FLX}^{red} = 0.4 Gg I/year for the SH and D_{FLX}^{red} = 0.1 Gg I/year for the NH). The reduced HI deposition can be explained by the small HI partitioning within the total inorganic iodine, which is comparatively much smaller than the equivalent HBr and HCl fractions within the bromine and chlorine families: HCl (HBr) is the most (second most) abundant inorganic chlorine (bromine) species in the MBL (Fernandez et al., 2014; Saiz-Lopez et al., 2014). Note that the model implementation of heterogeneous recycling was performed considering an infinite halide reservoir prevailing on top of the sea-ice; thus, the mass imbalance between D_{FLX}^{red} and D_{FLX}^{ox} for iodine compounds does not represent a technical limitation to the polar module configuration. However, this imbalance highlights the importance of including additional activation processes in the model to compensate for the additional sea-ice iodide content required for maintaining the efficiency of the heterogeneous recycling mechanism. For example, it has been suggested that (i) a fraction of the aqueous iodide and tri-iodide ions biologically produced underneath the sea-ice can contribute, in addition to the F_{ICE}^{I2} gas-phase flux, to refill and maintain the iodide abundance on top of the sea-ice surface (Saiz-Lopez, Boxe, et al., 2015); and (ii) nitrite mediated reduction of iodate ions can result in iodide formation within the ice grain boundaries (Kim et al., 2019). These assumptions explain the larger surface recycling efficiency for Antarctica, where the more porous and thin ice enhances the brine diffusion rates of inorganic iodine.

The $VSL^{PM\text{-}ind}$ experiment show that both the absolute recycling flux and the percentage contribution of each channel are strongly affected by the omission of the initial sea-ice sources (F_{ICE}). In the SH, the overall recycling flux is reduced by a factor of approximately 2, 4, and 12 for chlorine, bromine, and iodine, respectively (Table 6), highlighting the importance of F_{ICE} as a requirement for the initial release of gaseous halogen species, which can later be deposited and recycled back to the atmosphere. It also indicates the greater recycling efficiency of iodine with respect to bromine and chlorine on a per atom basis. For the NH, equivalent decreases in F_{HET}^{XY} strength are predicted for bromine and chlorine within the $VSL^{PM\text{-}ind}$ experiment. That is not the case for F_{HET}^{I}, which shows equivalent results for $VSL^{PM\text{-}on}$ and $VSL^{PM\text{-}ind}$, because the dominant iodine source in the Arctic is the ocean (F_{OCN}^{I} = 27.0 Gg I/year versus F_{ICE}^{I2} = 3×10^{-2} Gg I/year). We find that due to the large decrease in the bromine source in the $VSL^{PM\text{-}ind}$ simulation, chlorine reemission in the form of Cl_2 is at least twofold compared to the $VSL^{PM\text{-}on}$ case (see Table S4). As a consequence, the computed depositional fluxes for $ClONO_2$ and HOCl (D_{FLX}^{ox}) within the $VSL^{PM\text{-}ind}$ scheme always fulfill the chlorine mass balance required at the sea-ice surface. For the case of bromine, the less efficient recycling produces a shift in the dominant species being deposited on the sea-ice in the NH: within the $VSL^{PM\text{-}on}$ experiment, D_{FLX}^{red} is almost two times larger than D_{FLX}^{ox}, while for the $VSL^{PM\text{-}ind}$ experiment $D_{FLX}^{red} < D_{FLX}^{ox}$. Table S4 also indicates that for both experiments molecular bromine dominates the percentage contribution of the recycling process: the modeled Br_2 release represents ~70% of the total F_{HET}^{Br} both in the Arctic and Antarctica. That is not the case for chlorine, where the contribution from BrCl dominates the total surface recycling flux, representing ~75% of the

chlorine recycling emission and ~25% of the bromine mass release. This responds to the much larger deposition rate of oxidized bromine species with respect to their equivalent chlorinated species.

5.4. Quantification of Polar NO$_x$ Sources

The additional photochemical NO$_x$ source for each polar region is depicted in Figure S6 and quantified in Table S5 of the supporting information. The NO$_2$ surface flux (F_{NO2}) in Antarctica reaches 94 Gg N/year, while for the Arctic is approximately 44 Gg N/year. In order to compare the NO$_2$ polar emissions to other nitrogen sources, we have also quantified the polar NO anthropogenic emissions implemented in the benchmark CAM-Chem setup (Lamarque et al., 2012). Notably, while there are not any anthropogenic NO sources implemented for latitudes poleward of 50°S in the SH, within the NH polar cap the human-induced NO flux surpasses the sea-ice NO$_2$ source. Indeed, results for NO indicate that more than half of the nitrogen source in the NH polar cap is anthropogenic (ice-masked F_{NO} = 94 Gg N/year, while if the oceanic and continental anthropogenic sources are included, it rises up to 5.3 Tg N/year). The sea-ice release is the only nitrogen source in Antarctica (Wolff, 2013), and its inclusion affects background ozone levels and considerably changes the NO/NO$_2$ ratio, which in turn is correlated with the bromine and iodine halogen cycles through XONO$_2$ and XNO$_2$ formation (Bauguitte et al., 2012; Bloss et al., 2010). The percentage contribution of F_{NO2} during December–February, March–May, June–August, and September–November for Antarctica reaches 48%, 7%, 4%, and 41%, while for the Arctic it is 3%, 41%, 51%, and 5%, respectively.

5.5. Comparison of Polar Halogen Sources in Antarctica and the Arctic

Figure 12 presents the annual seasonal cycle for all considered halogen polar sources for the Arctic and Antarctica, while the percentage distribution of all sources during each season with respect to the annual mean is summarized in Table S6. The contribution of the bromine, chlorine, and iodine sea-ice fluxes peaks during austral midspring in Antarctica (October), while for the Arctic, the highest emissions are modeled in the late spring (May) for chlorine and bromine and in the summer (July) for iodine. The overall Antarctic bromine source shows a strong seasonality with maximum values of ~55 Gg Br/month in the late austral spring, as a compromise between the still large sea-ice coverage and the increasing rate of incident radiation. Note that even though the intensity of radiation is highest during the summer (Figure 4), the total first-year sea-ice (*newice*) extent peaks in late spring and reaches a summer minimum due to the higher temperatures, thereby reducing the overall halogen emission. This is partially compensated by the contribution of *meltice*, which is less important during spring and maximizes in the summer. F_{ICE} and F_{HET} contribute to the total surface flux with similar seasonality (~50% of the annual emission occurs during austral spring, 35% during the summer, and the remaining 15% during fall and winter), although in absolute values F_{ICE} represents more than 60% of the total bromine surface source. Indeed, F_{POLAR} represents the dominant source controlling the inorganic halogen abundance at the polar surface. Note that the overall contribution from sea-salt recycling integrated within the tropospheric column in Antarctica shows a similar seasonality as the one computed for the surface sources, with a nonnegligible background contribution during the summer and fall due to the large sea-salt aerosol production over the Southern Ocean. Equivalent total SSA enhancements on top of the dominant sea-ice source are modeled for the Arctic during boreal spring, although it rapidly disappears moving into the boreal fall and winter.

For chlorine, even when the sea-salt flux in the MBL still lies below the contribution from the sea-ice sources, the total column ($F_{SSA}^{trop} \approx 85.6$ Gg Cl/year for Antarctica and 68.0 Gg Cl/year for the Arctic) largely surpasses the overall surface sea-ice flux ($F_{POLAR}^{srf} \approx 31.9$ Gg Cl/year for the SH and 32.5 Gg Cl/year for the NH). Note that the minimum in sea-salt recycling and bromine SSA dehalogenation efficiency in the NH occurs during the late summer and fall (Table S6). The annual total flux considering all sea-ice sources released from each polar region reaches 31.9 Gg Cl/year and 249.9 Gg Br/year for Antarctica and 32.5 Gg Cl/year and 270.6 Gg Br/year for the Arctic. Added together, these sources represent, respectively, ~45% and ~80% of the global biogenic VSL chlorine and bromine emissions implemented in the model.

For the case of iodine, the seasonal variation follows the results obtained for bromine and chlorine, but with a more pronounced springtime enhancement due to the biologically induced source in Antarctica (Figure 12). Indeed, approximately 8 Gg I/month are emitted from the sea-ice surface during October, with ~90% of the total annual emission occurring during austral spring and summer (Table S6). We find that the efficient heterogeneous recycling of gas-phase reservoirs and sea-salt iodine over the snowpack is capable of
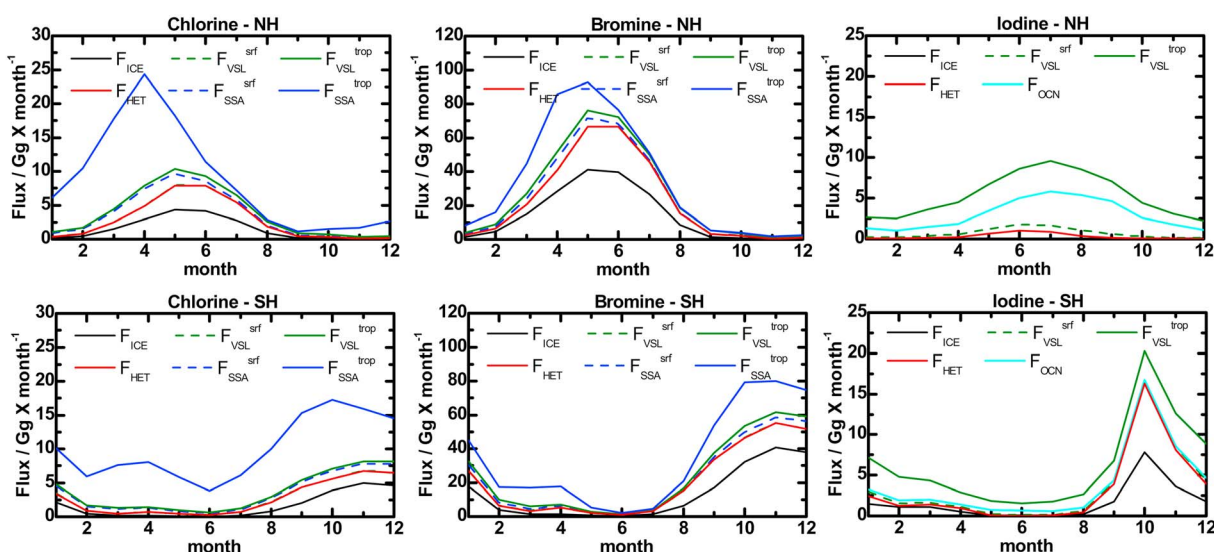
Figure 12. Annual seasonal cycle of the sea-ice (F_{ICE}) and heterogeneous (F_{HET}) emissions from the polar surface, VSL photodecomposition (F_{VSL}) and sea-salt recycling (F_{SSA}) sources. Each panel shows the flux strength of each individual source for chlorine (left), bromine (middle) and iodine (right) within the Arctic (top) and Antarctica (bottom). The total seasonal flux has been computed by adding the contribution of each independent source (one at a time for each colored line) in the following order: Flux $= F_{ICE} + F_{HET} + F_{OCN}^{I} + F_{VSL}^{srf} + F_{SSA}^{srf} + F_{VSL}^{trop} + F_{SSA}^{trop}$. The overall annual emissions and the percentage contribution within each season are given in Tables 5 and S6, respectively.

transporting active iodine from the Antarctic coast into the continent (Figure 11). Within the Arctic, the thicker sea-ice coverage blocks the direct emission of iodine from underneath the sea-ice, and the open water ocean source dominates over the other sources such as the heterogeneous recycling flux. Due to the sea-ice shrinkage and the larger open water extent during summer, F_{OCN}^{I} maximizes in July and represents the dominant iodine source to the Arctic atmosphere. The contribution from iodocarbon photodecomposition is the second largest in the NH when integrated throughout the tropospheric column. Note that SSA dehalogenation does not constitute an additional iodine source within our modeling approach, and thus sea-salt recycling only represents a change in partitioning for iodine.

6. Summary and Conclusions

The implementation of a novel polar module in CAM-Chem, considering inorganic halogen (Cl, Br, and I) emissions from the sea-ice surface and the heterogeneous recycling of reservoir species, provides a truly global representation of halogen chemistry within the troposphere. Indeed, to our knowledge, this is the first global model that includes a complete representation of all chlorine, bromine, and iodine sources and chemistry from pole-to-pole, and expanding from the Earth's surface up to the stratopause. Even though the parameterized implementation of the natural physicochemical processes releasing inorganic halogens to the polar troposphere has been performed in a simplified manner, it constitutes an improvement upon previous modeling approaches. The CAM-Chem polar module considers the online coupling between halogen emissions and their geophysical drivers such as ice coverage (*icefrac* and *newice*), intensity of radiation (i.e., cos (*SZA*)) and the influence of marine biological activity (*chl$_a$* satellite maps). This work also provides, for the first time, quantitative estimates of polar halogen emissions and their contribution to the global tropospheric halogen budget. The implementation of the polar module in CAM-Chem will allow to study the influence of natural halogens on chemistry-climate interactions and feedbacks.

The new polar module has been validated against surface and column-integrated observations of polar reactive halogens. The overall model performance shows consistent results both in the Arctic and Antarctica, with a model-observations bias that is smaller than the observed and modeled standard deviation. It is worth noting that, as the model considered meteorological conditions representative of the 2000th decade (i.e., it was not configured to follow a specified dynamics approach based on reanalysis data), we do not expect the model to present a perfect timing nor an exact spatial colocation for each

and all of the halogen field observations reported in the literature. Modeling the spatial and temporal features observed from satellites is especially challenging because model output and observations are not expected to show a one-to-one agreement due to albedo variations, which are not included in the satellite data retrieval. Instead, we focus our development on obtaining an adequate statistical validation of surface and satellite halogen observations throughout the polar troposphere, capable of reproducing the monthly mean and maximum values, as well as the relative distributions of chlorine, bromine, and iodine within the Arctic and Antarctica. In order to reproduce the satellite observations of IO over inner Antarctica, an iodine "leapfrog" mechanism is proposed to transport active iodine from coastal source regions to the interior of the continent.

The total source of chlorine and bromine in Antarctica is modeled to be 32 and 250 Gg/year, respectively, of which approximately 50% (35%) of the annual flux occurs during spring (summer). In comparison, approximately 45% of the modeled bromine and chlorine emissions from the Arctic occur during the summer, accounting for a total flux of 33 Gg Cl/year and 271 Gg Br/year, respectively. The distinct behavior of polar sources between the Arctic and Antarctica is attributed to the fact that the Arctic has a more concentrated poleward sea-ice distribution with large multiyear sea-ice areas; while in Antarctica, a comparatively larger irradiance reaches the summer sea-ice boundary at lower latitudes closer to the Antarctic polar circle. On average, the polar sources represent between 45 to 80% of the global biogenic VSL chlorine and bromine emissions, respectively. In contrast to bromine and chlorine, the modeled annual iodine emission strength in Antarctica is ~10 times larger than that in the Arctic. The notable difference in sea-ice thickness and permeability between the Arctic and Antarctic sea-ice drives polar surface emissions (39 Gg I/year) to dominate the inorganic iodine flux within the SH polar cap, while in the NH the polar module accounts only for 4 Gg I/year and the oceanic release of inorganic iodine constitutes the most important source (F_{OCN}^{I} = 27 Gg I/year). Marked geographical and seasonal features are modeled for iodine emissions, due to the parameterized dependence on the biological activity of algae colonies occurring underneath the sea-ice. Finally, our results highlight the importance of including an explicit treatment of polar halogen sources and chemistry in global models.

References

Abbatt, J. P. D., Thomas, J. L., Abrahamsson, K., Boxe, C., Granfors, A., Jones, A. E., et al. (2012). Halogen activation via interactions with environmental ice and snow in the polar lower troposphere and other regions. *Atmospheric Chemistry and Physics*, *12*(4), 8677–8769. https://doi.org/10.5194/acpd-12-8677-2012

Afe, O. T., Richter, A., Sierk, B., Wittrock, F., & Burrows, J. P. (2004). BrO emission from volcanoes: A survey using GOME and SCIAMACHY measurements. *Geophysical Research Letters*, *31*, L24113. https://doi.org/10.1029/2004GL020994

Artiglia, L., Edebeli, J., Orlando, F., Chen, S., Lee, M. T., Corral Arroyo, P., et al. (2017). A surface-stabilized ozonide triggers bromide oxidation at the aqueous solution-vapour interface. *Nature Communications*, *8*(1), 700–707. https://doi.org/10.1038/s41467-017-00823-x

Aschmann, J., Sinnhuber, B.-M., Atlas, E. L., & Schauffler, S. M. (2009). Modeling the transport of very short-lived substances into the tropical upper troposphere and lower stratosphere. *Atmospheric Chemistry and Physics*, *9*(23), 9237–9247. https://doi.org/10.5194/acp-9-9237-2009

Atkinson, H. M., Huang, R.-J., Chance, R., Roscoe, H. K., Hughes, C., Davison, B., et al. (2012). Iodine emissions from the sea ice of the Weddell Sea. *Atmospheric Chemistry and Physics*, *12*(5), 11,595–11,639. https://doi.org/10.5194/acpd-12-11595-2012

Atkinson, R., Baulch, D. L., Cox, R. A., Crowley, J. N., Hampson, R. F., Hynes, R. G., et al. (2007). Evaluated kinetic and photochemical data for atmospheric chemistry: Volume III—Gas phase reactions of inorganic halogens. *Atmospheric Chemistry and Physics*, *7*(4), 981–1191. https://doi.org/10.5194/acp-7-981-2007

Atkinson, R., Baulch, D. L., Cox, R. A., Crowley, J. N., Hampson, R. F., Hynes, R. G., et al. (2008). Evaluated kinetic and photochemical data for atmospheric chemistry: Volume IV—Gas phase reactions of organic halogen species. *Atmospheric Chemistry and Physics*, *8*(15), 4141–4496. https://doi.org/10.5194/acp-8-4141-2008

Barrie, L. A., Bottenheim, J. W., Schnell, R. C., Crutzen, P. J., & Rasmussen, R. A. (1988). Ozone destruction and photochemical reactions at polar sunrise in the lower Arctic atmosphere. *Nature*, *332*(6160), 141–142. https://doi.org/10.1038/332141a0

Bauguitte, S. J. B., Bloss, W. J., Evans, M. J., Salmon, R. A., Anderson, P. S., Jones, A. E., et al. (2012). Summertime NOx measurements during the CHABLIS campaign: Can source and sink estimates unravel observed diurnal cycles? *Atmospheric Chemistry and Physics*, *12*(2), 989–1002. https://doi.org/10.5194/acp-12-989-2012

Begoin, M., Richter, A., Weber, M., Kaleschke, L., Tian-Kunze, X., Stohl, A., et al. (2010). Satellite observations of long range transport of a large BrO plume in the Arctic. *Atmospheric Chemistry and Physics*, *10*(14), 6515–6526. https://doi.org/10.5194/acp-10-6515-2010

Blechschmidt, A.-M., Richter, A., Burrows, J. P., Kaleschke, L., Strong, K., Theys, N., et al. (2016). An exemplary case of a bromine explosion event linked to cyclone development in the Arctic. *Atmospheric Chemistry and Physics*, *16*(3), 1773–1788. https://doi.org/10.5194/acp-16-1773-2016

Bloss, W. J., Camredon, M., Lee, J. D., Heard, D. E., Plane, J. M. C., Saiz-Lopez, A., et al. (2010). Coupling of HOx, NOx and halogen chemistry in the antarctic boundary layer. *Atmospheric Chemistry and Physics*, *10*(21), 10,187–10,209. https://doi.org/10.5194/acp-10-10187-2010

Bottenheim, J. W., & Gallant, A. G. (1986). Measurements of NOy species and 03 at 82°N latitude. *Geophysical Research Letters*, *13*(2), 113–116. https://doi.org/10.1029/GL013i002p00113

Bovensmann, H., Burrows, J. P., Buchwitz, M., Frerick, J., Noël, S., Rozanov, V. V., et al. (1999). SCIAMACHY: Mission objectives and measurement modes. *Journal of the Atmospheric Sciences*, *56*(2), 127–150. https://doi.org/10.1175/1520-0469(1999)056<0127: SMOAMM>2.0.CO;2

Boxe, C. S., & Saiz-Lopez, A. (2008). Multiphase modeling of nitrate photochemistry in the quasi-liquid layer (QLL): Implications for NOx release from the Arctic and coastal Antarctic snowpack. *Atmospheric Chemistry and Physics*, *8*(16), 4855–4864. https://doi.org/10.5194/acp-8-4855-2008

Brooks, S. B., Saiz-Lopez, A., Skov, H., Lindberg, S. E., Plane, J. M. C., & Goodsite, M. E. (2006). The mass balance of mercury in the springtime Arctic environment. *Geophysical Research Letters*, *33*, L13812. https://doi.org/10.1029/2005GL025525

Burrows, J. P., Hölzle, E., Goede, A. P. H., Visser, H., & Fricke, W. (1995). SCIAMACHY-scanning imaging absorption spectrometer for atmospheric chartography. *Acta Astronautica*, *35*(7), 445–451. https://doi.org/10.1016/0094-5765(94)00278-T

Callies, J., Corpaccioli, E., Eisinger, M., Hahne, A., & Lefebvre, A. (2000). GOME-2—Metop's second-generation sensor for operational ozone monitoring. ESA Bulletin-European Space Agency, 102(may), 28–36.

Carpenter, L. J., MacDonald, S. M., Shaw, M. D., Kumar, R., Saunders, R. W., Parthipan, R., et al. (2013). Atmospheric iodine levels influenced by sea surface emissions of inorganic iodine. *Nature Geoscience*, *6*(2), 108–111. https://doi.org/10.1038/ngeo1687

CISL. (2017). Computational and Information Systems Laboratory. Cheyenne: HPE/SGI ICE XA System (NCAR Community Computing), Boulder, CO, USA: National Center for Atmospheric Research (NCAR). https://doi.org/10.5065/D6RX99HX

Cuevas, C. A., Maffezzoli, N., Corella, J. P., Spolaor, A., Vallelonga, P., Kjær, H. A., et al. (2018). Rapid increase in atmospheric iodine levels in the North Atlantic since the mid-20th century. *Nature Communications*, *9*(1), 1452–1456. https://doi.org/10.1038/s41467-018-03756-1

Domine, F., Albert, M., Huthwelker, T., Jacobi, H.-W., Kokhanovsky, A. A., Lehning, M., et al. (2008). Snow physics as relevant to snow photochemistry. *Atmospheric Chemistry and Physics*, *8*(2), 171–208. https://doi.org/10.5194/acp-8-171-2008

Dominé, F., & Shepson, P. B. (2002). Air-snow interactions and atmospheric chemistry. *Science*, *297*(5586), 1506–1510. https://doi.org/10.1126/science.1074610

Dorf, M., Butz, A., Camy-Peyret, C., Chipperfield, M. P., Kritten, L., & Pfeilsticker, K. (2008). Bromine in the tropical troposphere and stratosphere as derived from balloon-borne BrO observations. *Atmospheric Chemistry and Physics*, *8*(4), 12,999–13,015. https://doi.org/10.5194/acpd-8-12999-2008

Emmons, L. K., Walters, S., Hess, P. G., Lamarque, J.-F., Pfister, G. G., Fillmore, D., et al. (2010). Description and evaluation of the model for ozone and related chemical tracers, version 4 (MOZART-4). *Geoscientific Model Development*, *3*(1), 43–67. https://doi.org/10.5194/gmd-3-43-2010

Evans, M. J. (2003). Coupled evolution of BrO_x -ClO_x -HO_x -NO_x chemistry during bromine-catalyzed ozone depletion events in the arctic boundary layer. *Journal of Geophysical Research*, *108*(D4), 8368. https://doi.org/10.1029/2002JD002732

Falk, S., Sinnhuber, B.-M. (2018). Polar boundary layer bromine explosion and ozone depletion events in the chemistry-climate model EMAC v2.52: Implementation and evaluation of AirSnow algorithm. *Geoscientific Model Development*, 1115–1131. https://doi.org/10.5194/gmd-11-1115-2018

Fan, S. M., & Jacob, D. J. (1992). Surface ozone depletion in Arctic spring sustained by bromine reactions on aerosols. *Nature*, *359*(6395), 522–524. https://doi.org/10.1038/359522a0

Fernandez, R., Salawitch, R., Kinnison, D., Lamarque, J., & Saiz-Lopez, A. (2014). Bromine partitioning in the tropical tropopause layer: Implications for stratospheric injection. *Atmospheric Chemistry and Physics*, *14*(24), 391–410. https://doi.org/10.5194/acp-14-13391-2014

Fernandez, R. P., Kinnison, D. E., Lamarque, J.-F., Tilmes, S., & Saiz-Lopez, A. (2017). Impact of biogenic very short-lived bromine on the Antarctic ozone hole during the 21st century. *Atmospheric Chemistry and Physics*, 1673–1688. https://doi.org/10.5194/acp-2016-840

Fernandez, R. P., Salawitch, R. J., Kinnison, D. E., Lamarque, J.-F., & Saiz-Lopez, A. (2014). Bromine partitioning in the tropical tropopause layer: implications for stratospheric injection. *Atmospheric Chemistry and Physics*, *14*(24), 13,391–13,410. https://doi.org/10.5194/acp-14-13391-2014

Foster, K. L., Plastridge, R. A., Bottenheim, J. W., Shepson, P. B., Finlayson-Pitts, B. J., & Spicer, C. W. (2001). The role of Br2 and BrCl in surface ozone destruction at polar sunrise. *Science*, *291*(5503), 471–474. https://doi.org/10.1126/science.291.5503.471

Gálvez, Ó., Baeza-romero, M. T., Sanz, M., & Saiz-lopez, A. (2016). Photolysis of frozen iodate salts as a source of active iodine in the polar environment. *Atmospheric Chemistry and Physics*, *16*, 12,703–12,713. https://doi.org/10.5194/acp-16-12703-2016

Goodsite, M. E., Plane, J. M. C., & Skov, H. (2004). A theoretical study of the oxidation of Hg^0 to $HgBr_2$ in the troposphere. *Environmental Science & Technology*, *38*(6), 1772–1776. https://doi.org/10.1021/es034680s

Hay, T. D. (2011). *MAX-DOAS Measurements of Bromine Explosion Events in McMurdo Sound, Antarctica*. New Zealand: University of Canterbury.

Hossaini, R., Chipperfield, M. P., Monge-Sanz, B. M., Richards, N. A. D., Atlas, E., Blake, D. R., & Science, A. (2010). Bromoform and dibromomethane in the tropics: A 3-D model study of chemistry and transport. *Atmospheric Chemistry and Physics*, *10*(2), 719–735. https://doi.org/10.5194/acp-10-719-2010

Hossaini, R., Chipperfield, M. P., Saiz-Lopez, A., Fernandez, R., Monks, S., Brauer, P., & von Glasow, R. (2016). A global model of tropospheric chlorine chemistry: Organic versus inorganic sources and impact on methane oxidation. *Journal of Geophysical Research: Atmospheres*, *121*, 14,271–14,297. https://doi.org/10.1002/2016JD025756

Jones, A. E., Anderson, P. S., Begoin, M., Brough, N., Hutterli, M. A., Marshall, G. J., et al. (2009). BrO, blizzards, and drivers of polar tropospheric ozone depletion events. *Atmospheric Chemistry and Physics*, *9*(14), 4639–4652. https://doi.org/10.5194/acp-9-4639-2009

Jones, A. E., Wolff, E. W., Ames, D., Bauguitte, S. J. B., Clemitshaw, K. C., Fleming, Z., et al. (2011). The multi-seasonal NOy budget in coastal Antarctica and its link with surface snow and ice core nitrate: Results from the CHABLIS campaign. *Atmospheric Chemistry and Physics*, *11*(17), 9271–9285. https://doi.org/10.5194/acp-11-9271-2011

Kim, K., Ju, J., Kim, B., Chung, H. Y., Vetráková, L.'., Heger, D., et al. (2019). Nitrite-induced activation of iodate into molecular iodine in frozen solution. *Environmental Science & Technology*, *53*(9), 4892–4900. https://doi.org/10.1021/acs.est.8b06638

Kim, K., Yabushita, A., Okumura, M., Saiz-Lopez, A., Cuevas, C. A., Blaszczak-Boxe, C. S., et al. (2016). Production of molecular iodine and tri-iodide in the frozen solution of iodide: implication for polar atmosphere. *Environmental Science & Technology*, *50*(3), 1280–1287. https://doi.org/10.1021/acs.est.5b05148

Kinnison, D. E., Brasseur, G. P., Walters, S., Garcia, R. R., Marsh, D. R., Sassi, F., et al. (2007). Sensitivity of chemical tracers to meteorological parameters in the MOZART-3 chemical transport model. *Journal of Geophysical Research*, *112*, D20302. https://doi.org/10.1029/2006JD007879

Lamarque, J.-F., Emmons, L. K., Hess, P. G., Kinnison, D. E., Tilmes, S., Vitt, F., et al. (2012). CAM-Chem: Description and evaluation of interactive atmospheric chemistry in the Community Earth System Model. *Geoscientific Model Development*, *5*(2), 369–411. https://doi.org/10.5194/gmd-5-369-2012

Lawler, M. J., Mahajan, A. S., Saiz-Lopez, A., & Saltzman, E. S. (2014). Observations of I₂ at a remote marine site. *Atmospheric Chemistry and Physics*, *14*(5), 2669–2678. https://doi.org/10.5194/acp-14-2669-2014

Lehrer, E., Hönninger, G., & Platt, U. (2004). A one-dimensional model study of the mechanism of halogen liberation and vertical transport in the polar troposphere. *Atmospheric Chemistry and Physics*, *4*(11/12), 2427–2440. https://doi.org/10.5194/acp-4-2427-2004

Liang, Q., Atlas, E., Blake, D., Dorf, M., Pfeilsticker, K., & Schauffler, S. (2014). Convective transport of very short lived bromocarbons to the stratosphere. *Atmospheric Chemistry and Physics*, *14*(11), 5781–5792. https://doi.org/10.5194/acp-14-5781-2014

Liang, Q., Stolarski, R. S., Kawa, S. R., Nielsen, J. E., Douglass, A. R., Rodriguez, J. M., et al. (2010). Finding the missing stratospheric Brᵧ: A global modeling study of CHBr₃ and CH₂Br₂. *Atmospheric Chemistry and Physics*, *10*(5), 2269–2286. https://doi.org/10.5194/acp-10-2269-2010

Liao, J., Huey, L. G., Liu, Z., Tanner, D. J., Cantrell, C. A., Orlando, J. J., et al. (2014). High levels of molecular chlorine in the Arctic atmosphere. *Nature Geoscience*, *7*(2), 91–94. https://doi.org/10.1038/ngeo2046

Liao, J., Huey, L. G., Tanner, D. J., Flocke, F. M., Orlando, J. J., Neuman, J. A., et al. (2012). Observations of inorganic bromine (HOBr, BrO, and Br2) speciation at Barrow, Alaska, in spring 2009. *Journal of Geophysical Research*, *117*, D00R16. https://doi.org/10.1029/2011JD016641

MacDonald, S. M., Gómez Martín, J. C., Chance, R., Warriner, S., Saiz-Lopez, A., Carpenter, L. J., & Plane, J. M. C. (2014). A laboratory characterisation of inorganic iodine emissions from the sea surface: dependence on oceanic variables and parameterisation for global modelling. *Atmospheric Chemistry and Physics*, *14*(11), 5841–5852. https://doi.org/10.5194/acp-14-5841-2014

Mahajan, A. S., Plane, J. M. C., Oetjen, H., Mendes, L., Saunders, R. W., Saiz-Lopez, A., et al. (2010). Measurement and modelling of tropospheric reactive halogen species over the tropical Atlantic Ocean. *Atmospheric Chemistry and Physics*, *10*(10), 4611–4624. https://doi.org/10.5194/acp-10-4611-2010

Mahajan, A. S., Shaw, M., Oetjen, H., Hornsby, K. E., Carpenter, L. J., Kaleschke, L., et al. (2010). Evidence of reactive iodine chemistry in the Arctic boundary layer. *Journal of Geophysical Research*, *115*, D20303. https://doi.org/10.1029/2009JD013665

Mahajan, A. S., Sorribas, M., Gómez Martín, J. C., MacDonald, S. M., Gil, M., Plane, J. M. C., & Saiz-Lopez, A. (2011). Concurrent observations of atomic iodine, molecular iodine and ultrafine particles in a coastal environment. *Atmospheric Chemistry and Physics*, *11*(6), 2545–2555. https://doi.org/10.5194/acp-11-2545-2011

Mahowald, N. M., Lamarque, J.-F., Tie, X. X., & Wolff, E. (2006). Sea-salt aerosol response to climate change: Last Glacial Maximum, preindustrial, and doubled carbon dioxide climates. *Journal of Geophysical Research*, *111*, D05303. https://doi.org/10.1029/2005JD006459

Martinez, M., Arnold, T., & Perner, D. (1999). The role of bromine and chlorine chemistry for arctic ozone depletion events in Ny-Ålesund and comparison with model calculations. *Annales Geophysicae*, *17*(7), 941–956. https://doi.org/10.1007/s00585-999-0941-4

McFiggans, G., Plane, J. M. C., Allan, B. J., Carpenter, L. J., Coe, H., & O'Dowd, C. (2000). A modeling study of iodine chemistry in the marine boundary layer. *Journal of Geophysical Research*, *105*(D11), 14,371–14,385. https://doi.org/10.1029/1999JD901187

Meinshausen, M., Smith, S. J., Calvin, K., Daniel, J. S., Kainuma, M. L. T., Lamarque, J.-F., et al. (2011). The RCP greenhouse gas concentrations and their extensions from 1765 to 2300. *Climatic Change*, *109*(1–2), 213–241. https://doi.org/10.1007/s10584-011-0156-z

Monahan, E. C., Spiel, D. E., & Davidson, K. L. (1986). *A Model of Marine Aerosol Generation Via Whitecaps and Wave Disruption*, (pp. 167–174). Dordrecht: Springer. https://doi.org/10.1007/978-94-009-4668-2_16

Murphy, D. M., Froyd, K. D., Bian, H., Brock, C. A., Dibb, J. E., DiGangi, J. P., et al. (2018). The distribution of sea-salt aerosol in the global troposphere. *Atmospheric Chemistry and Physics Discussions*, 1–27. https://doi.org/10.5194/acp-2018-1013

Navarro, M. A., Atlasa, E. L., Saiz-Lopez, A., Rodriguez-Lloveras, X., Kinnison, D. E., Lamarque, J.-F., et al. (2015). Airborne measurements of organic bromine compounds in the Pacific tropical tropopause layer. *Proceedings of the National Academy of Sciences of the United States of America*, *112*(45), 13,789–13,793. https://doi.org/10.1073/pnas.1522889113

Navarro, M. A., Saiz-Lopez, A., Cuevas, C. A., Fernandez, R. P., Atlas, E., Rodriguez-Lloveras, X., et al. (2017). Modeling the inorganic bromine partitioning in the tropical tropopause layer over the eastern and western Pacific Ocean. *Atmospheric Chemistry and Physics*, *17*, 9917–9930. https://doi.org/10.5194/acp-17-9917-2017

O'Driscoll, P., Lang, K., Minogue, N., & Sodeau, J. (2006). Freezing halide ion solutions and the release of interhalogens to the atmosphere. *Journal of Physical Chemistry A*, *110*(14), 4615–4618. https://doi.org/10.1021/jp060491v

O'Driscoll, P., Minogue, N., Takenaka, N., & Sodeau, J. (2008). Release of nitric oxide and iodine to the atmosphere from the freezing of sea-salt aerosol components. *Journal of Physical Chemistry A*, *112*(8), 1677–1682. https://doi.org/10.1021/jp710464c

Oltmans, S. J., & Komhyr, W. D. (1986). Surface ozone distributions and variations from 1973–1984: Measurements at the NOAA geophysical monitoring for climatic change baseline observatories. *Journal of Geophysical Research*, *91*(D4), 5229–5236. https://doi.org/10.1029/JD091iD04p05229

Oman, L. D., Douglass, A. R., Salawitch, R. J., Canty, T. P., Ziemke, J. R., & Manyin, M. (2016). The effect of representing bromine from VSLS on the simulation and evolution of Antarctic ozone. *Geophysical Research Letters*, *43*, 9869–9876. https://doi.org/10.1002/2016GL070471

Ordóñez, C., Lamarque, J.-F., Tilmes, S., Kinnison, D. E., Atlas, E. L., Blake, D. R., et al. (2012). Bromine and iodine chemistry in a global chemistry-climate model: Description and evaluation of very short-lived oceanic sources. *Atmospheric Chemistry and Physics*, *12*(3), 1423–1447. https://doi.org/10.5194/acp-12-1423-2012

O'Sullivan, D., & Sodeau, J. R. (2010). Freeze-induced reactions: Formation of iodine−bromine interhalogen species from aqueous halide ion solutions. *The Journal of Physical Chemistry A*, *114*(46), 12,208–12,215. https://doi.org/10.1021/jp104910p

Parrella, J. P., Jacob, D. J., Liang, Q., Zhang, Y., Mickley, L. J., Miller, B., et al. (2012). Tropospheric bromine chemistry: Implications for present and pre-industrial ozone and mercury. *Atmospheric Chemistry and Physics*, *12*(15), 6723–6740. https://doi.org/10.5194/acp-12-6723-2012

Plane, J., & Saiz-Lopez, A. (2006). UV-Visible differential optical absorption spectroscopy (DOAS). In Analytical techniques for atmospheric measurement. Retrieved from http://books.google.com/books?hl=en&lr=&id=OO8Z78CJep8C&oi=fnd&pg=PA147&dq=UV-Visible+Differential+Optical+Absorption+Spectroscopy+(DOAS)&ots=8UJONCBZHy&sig=pZpDHddc17W1rMBXLdSHlqKCt_A

Platt, U. (1994). Differential optical absorption spectroscopy (doas). In M. W. Sigrist (Ed.), *Air Monitoring by Spectroscopic Techniques*, (pp. 27–84). New York: John Wiley.

Platt, U., & Stutz, J. (2008). Differential Absorption Spectroscopy. In *Differential Optical Absorption Spectroscopy*, (pp. 135–174). Berlin, Heidelberg: Springer. https://doi.org/10.1007/978-3-540-75776-4_6

Pöhler, D., Vogel, L., Friess, U., & Platt, U. (2010). Observation of halogen species in the Amundsen Gulf, Arctic, by active long-path differential optical absorption spectroscopy. *Proceedings of the National Academy of Sciences of the United States of America*, *107*(15), 6582–6587. https://doi.org/10.1073/pnas.0912231107

Prados-Roman, C., Cuevas, C. A., Fernandez, R. P., Kinnison, D. E., Lamarque, J. F., & Saiz-Lopez, A. (2015). A negative feedback between anthropogenic ozone pollution and enhanced ocean emissions of iodine. *Atmospheric Chemistry and Physics*, *15*(4), 2215–2224. https://doi.org/10.5194/acp-15-2215-2015

Prados-Roman, C., Cuevas, C. A., Hay, T., Fernandez, R. P., Mahajan, A. S., Royer, S.-J., et al. (2015). Iodine oxide in the global marine boundary layer. *Atmospheric Chemistry and Physics*, *15*(2), 583–593. https://doi.org/10.5194/acp-15-583-2015

Pratt, K. A., Custard, K. D., Shepson, P. B., Douglas, T. A., Pöhler, D., General, S., et al. (2013). Photochemical production of molecular bromine in Arctic surface snowpacks. *Nature Geoscience*, *6*(5), 351–356. https://doi.org/10.1038/ngeo1779

Raso, A. R. W., Custard, K. D., May, N. W., Tanner, D., Newburn, M. K., Walker, L., et al. (2017). Active molecular iodine photochemistry in the Arctic. *Proceedings of the National Academy of Sciences of the United States of America*, *114*(38), 10,053–10,058. https://doi.org/10.1073/pnas.1702803114

Rayner, N. A. (2003). Global analyses of sea surface temperature, sea ice, and night marine air temperature since the late nineteenth century. *Journal of Geophysical Research*, *108*(D14), 4407. https://doi.org/10.1029/2002JD002670

Read, K. A., Lewis, A. C., Bauguitte, S., Rankin, A. M., Salmon, R. A., Wolff, E. W., et al. (2008). DMS and MSA measurements in the Antarctic Boundary Layer: impact of BrO on MSA production. *Atmospheric Chemistry and Physics*, *8*(1), 2657–2694. https://doi.org/10.5194/acpd-8-2657-2008

Read, K. A., Mahajan, A. S., Carpenter, L. J., Evans, M. J., Faria, B. V. E., Heard, D. E., et al. (2008). Extensive halogen-mediated ozone destruction over the tropical Atlantic Ocean. *Nature*, *453*(7199), 1232–1235. https://doi.org/10.1038/nature07035

Saiz-Lopez, A., Baidar, S., Cuevas, C. A., Koenig, T. K., Fernandez, R. P., Dix, B., et al. (2015). Injection of iodine to the stratosphere. *Geophysical Research Letters*, *42*, 6852–6859. https://doi.org/10.1002/2015GL064796

Saiz-Lopez, A., & Blaszczak-Boxe, C. S. (2016). The polar iodine paradox. *Atmospheric Environment*, *145*, 72–73. https://doi.org/10.1016/j.atmosenv.2016.09.019

Saiz-Lopez, A., Boxe, C. S., & Carpenter, L. J. (2015). A mechanism for biologically induced iodine emissions from sea ice. *Atmospheric Chemistry and Physics*, *15*(17), 9731–9746. https://doi.org/10.5194/acp-15-9731-2015

Saiz-Lopez, A., & Fernandez, R. P. (2016). On the formation of tropical rings of atomic halogens: Causes and implications. *Geophysical Research Letters*, *43*, 2928–2935. https://doi.org/10.1002/2015GL067608

Saiz-Lopez, A., Fernandez, R. P., Ordóñez, C., Kinnison, D. E., Gómez Martín, J. C., Lamarque, J.-F., & Tilmes, S. (2014). Iodine chemistry in the troposphere and its effect on ozone. *Atmospheric Chemistry and Physics*, *14*(23), 13,119–13,143. https://doi.org/10.5194/acp-14-13119-2014

Saiz-Lopez, A., Lamarque, J.-F., Kinnison, D. E., Tilmes, S., Ordóñez, C., Orlando, J. J., et al. (2012). Estimating the climate significance of halogen-driven ozone loss in the tropical marine troposphere. *Atmospheric Chemistry and Physics*, *12*(9), 3939–3949. https://doi.org/10.5194/acp-12-3939-2012

Saiz-Lopez, A., Mahajan, A. S., Salmon, R. A., Bauguitte, S. J.-B., Jones, A. E., Roscoe, H. K., & Plane, J. M. C. (2007). Boundary layer halogens in coastal Antarctica. *Science*, *317*(5836), 348–351. https://doi.org/10.1126/science.1141408

Saiz-Lopez, A., Plane, J. M. C., Baker, A. R., Carpenter, L. J., von Glasow, R., Gómez Martín, J. C., et al. (2012). Atmospheric chemistry of iodine. *Chemical Reviews*, *112*(3), 1773–1804. https://doi.org/10.1021/cr200029u

Saiz-Lopez, A., Plane, J. M. C., Mahajan, A. S., Anderson, P. S., Bauguitte, S. J.-B., Jones, A. E., et al. (2008). On the vertical distribution of boundary layer halogens over coastal Antarctica: implications for O3, HOx, NOx and the Hg lifetime. *Atmospheric Chemistry and Physics*, *8*(4), 887–900. https://doi.org/10.5194/acp-8-887-2008

Saiz-Lopez, A., & von Glasow, R. (2012). Reactive halogen chemistry in the troposphere. *Chemical Society Reviews*, *41*(19), 6448–6472. https://doi.org/10.1039/c2cs35208g

Salawitch, R. J., Weisenstein, D. K., Kovalenko, L. J., Sioris, C. E., Wennberg, P. O., Chance, K., et al. (2005). Sensitivity of ozone to bromine in the lower stratosphere. *Geophysical Research Letters*, *32*, L05811. https://doi.org/10.1029/2004GL021504

Sander, S. P., Abbatt, J. P. D., Barker, J. R., Burkholder, J. B., Friedl, R. R., Golden, D. M., et al. (2010). Chemical kinetics and photochemical data for use in atmospheric studies, Evaluation Number 16. JPL_NASA, 09–31(16), 1–17.

Sander, S. P., Friedl, R. R., Barker, J. R., Golden, D. M., Kurylo, M. J., Sciences, G. E., et al. (2011). Chemical Kinetics and Photochemical Data for Use in Atmospheric Studies, Evaluation No. 17, JPL_NASA, 10–6(17), JetPropulsion Laboratory, Pasadena, CA.

Schönhardt, A., Begoin, M., Richter, A., Wittrock, F., Kaleschke, L., Gómez Martín, J. C., & Burrows, J. P. (2012). Simultaneous satellite observations of IO and BrO over Antarctica. *Atmospheric Chemistry and Physics*, *12*(14), 6565–6580. https://doi.org/10.5194/acp-12-6565-2012

Schönhardt, A., Richter, A., Wittrock, F., Kirk, H., Oetjen, H., Roscoe, H. K., & Burrows, J. P. (2008). Observations of iodine monoxide columns from satellite. *Atmospheric Chemistry and Physics*, *8*(3), 637–653. https://doi.org/10.5194/acp-8-637-2008

Sherwen, T., Schmidt, J. A., Evans, M. J., Carpenter, L. J., Großmann, K., Eastham, S. D., et al. (2016). Global impacts of tropospheric halogens (Cl, Br, I) on oxidants and composition in GEOS-Chem. *Atmospheric Chemistry and Physics*, *16*(18), 12,239–12,271. https://doi.org/10.5194/acp-16-12239-2016

Simpson, W. R., Brown, S. S., Saiz-Lopez, A., Thornton, J. A., & von Glasow, R. (2015). Tropospheric halogen chemistry: Sources, cycling, and impacts. *Chemical Reviews*, *115*(10), 4035–4062. https://doi.org/10.1021/cr5006638

Simpson, W. R., von Glasow, R., Riedel, K., Anderson, P., Ariya, P., Bottenheim, J., et al. (2007). Halogens and their role in polar boundary-layer ozone depletion. *Atmospheric Chemistry and Physics*, *7*(16), 4375–4418. https://doi.org/10.5194/acp-7-4375-2007

Sinnhuber, B.-M., & Folkins, I. (2006). Estimating the contribution of bromoform to stratospheric bromine and its relation to dehydration in the tropical tropopause layer. *Atmospheric Chemistry and Physics*, *6*(12), 4755–4761. https://doi.org/10.5194/acp-6-4755-2006

Skov, H., Christensen, J. H., Goodsite, M. E., Heidam, N. Z., Jensen, B., Wåhlin, P., & Geernaert, G. (2004). Fate of elemental mercury in the Arctic during atmospheric mercury depletion episodes and the load of atmospheric mercury to the Arctic. *Environmental Science and Technology*, *32*(7), 886–890. https://doi.org/10.1111/j.1524-4725.2006.32191.x

Smith, M. H., Park, P. M., & Consterdine, I. E. (1993). Marine aerosol concentrations and estimated fluxes over the sea. *Quarterly Journal of the Royal Meteorological Society*, *119*(512), 809–824. https://doi.org/10.1002/qj.49711951211

Steffen, A., Douglas, T., Amyot, M., Ariya, P., Aspmo, K., Berg, T., et al. (2007). A synthesis of atmospheric mercury depletion event chemistry linking atmosphere, snow and water. *Atmospheric Chemistry and Physics Discussions*, *7*(4), 10,837–10,931. https://doi.org/10.5194/acpd-7-10837-2007

Sturges, W. T., Sullivan, C. W., Schnell, R. C., Heidt, L. E., & Pollock, W. H. (1993). Bromoalkane production by Antarctic ice algae. *Tellus Series B: Chemical and Physical Meteorology*, *45*(2), 120–126. https://doi.org/10.1034/j.1600-0889.1993.t01-1-00004.x

Theys, N., van Roozendael, M., Errera, Q., Hendrick, F., Daerden, F., Chabrillat, S., et al. (2009). A global stratospheric bromine monoxide climatology based on the BASCOE chemical transport model. *Atmospheric Chemistry and Physics*, *9*(3), 831–848. https://doi.org/10.5194/acp-9-831-2009

Theys, N., van Roozendael, M., Hendrick, F., Yang, X., de Smedt, I., Richter, A., et al. (2011). Global observations of tropospheric BrO columns using GOME-2 satellite data. *Atmospheric Chemistry and Physics*, *11*(4), 1791–1811. https://doi.org/10.5194/acp-11-1791-2011

Thompson, C. R., Shepson, P. B., Liao, J., Huey, L. G., Apel, E. C., Cantrell, C. A., et al. (2015). Interactions of bromine, chlorine, and iodine photochemistry during ozone depletions in Barrow, Alaska. *Atmospheric Chemistry and Physics*, *15*(16), 9651–9679. https://doi.org/10.5194/acp-15-9651-2015

Tilmes, S., Lamarque, J. F., Emmons, L. K., Kinnison, D. E., Marsh, D., Garcia, R. R., et al. (2016). Representation of the Community Earth System Model (CESM1) CAM4-chem within the Chemistry-Climate Model Initiative (CCMI). *Geoscientific Model Development*, *9*(5), 1853–1890. https://doi.org/10.5194/gmd-9-1853-2016

Toyota, K., McConnell, J. C., Lupu, A., Neary, L., McLinden, C. A., Richter, A., et al. (2011). Analysis of reactive bromine production and ozone depletion in the Arctic boundary layer using 3-D simulations with GEM-AQ: Inference from synoptic-scale patterns. *Atmospheric Chemistry and Physics*, *11*(8), 3949–3979. https://doi.org/10.5194/acp-11-3949-2011

Tuckermann, M., Ackermann, R., Gölz, C., Lorenzen-Schmidt, H., Senne, T., Stutz, J., et al. (1997). DOAS-observation of halogen radical-catalysed arctic boundary layer ozone destruction during the ARCTOC-campaigns 1995 and 1996 in Ny-Ålesund, Spitsbergen. *Tellus Series B: Chemical and Physical Meteorology*, *49*(5), 533–555. https://doi.org/10.3402/tellusb.v49i5.16005

Vogt, R., Crutzen, P. J., & Sander, R. (1996). A mechanism for halogen release from sea-salt aerosol in the remote marine boundary layer. *Nature*, *383*(6598), 327–330. https://doi.org/10.1038/383327a0

Wang, S., & Pratt, K. A. (2017). Molecular halogens above the Arctic snowpack: Emissions, diurnal variations, and recycling mechanisms. *Journal of Geophysical Research: Atmospheres*, *122*, 11,991–12,007. https://doi.org/10.1002/2017JD027175

Wang, S., Schmidt, J. A., Baidar, S., Coburn, S., Dix, B., Koenig, T. K., et al. (2015). Active and widespread halogen chemistry in the tropical and subtropical free troposphere. *Proceedings of the National Academy of Sciences of the United States of America*, *112*(30), 9281–9286. https://doi.org/10.1073/pnas.1505142112

Wegner, T., Kinnison, D. E., Garcia, R. R., & Solomon, S. (2013). Simulation of polar stratospheric clouds in the specified dynamics version of the whole atmosphere community climate model. *Journal of Geophysical Research: Atmospheres*, *118*, 4991–5002. https://doi.org/10.1002/jgrd.50415

WMO. (2018). Scientific assessment of ozone depletion: 2018, Global Ozone Research and Monitoring Project-Report No 58. Geneva, Switzerland.

Wolff, E. W. (2013). Ice sheets and nitrogen. *Philosophical Transactions of the Royal Society of London. Series B, Biological Sciences*, *368*(1621), 20130127. https://doi.org/10.1098/rstb.2013.0127

Yang, X., Cox, R. A., Warwick, N. J., Pyle, J. A., Carver, G. D., O'Connor, F. M., & Savage, N. H. (2005). Tropospheric bromine chemistry and its impacts on ozone: A model study. *Journal of Geophysical Research*, *110*, D23311. https://doi.org/10.1029/2005JD006244

Yang, X., Pyle, J. A., Cox, R. A., Theys, N., & Van Roozendael, M. (2010). Snow-sourced bromine and its implications for polar tropospheric ozone. *Atmospheric Chemistry and Physics*, *10*(16), 7763–7773. https://doi.org/10.5194/acp-10-7763-2010

Erratum

Due to a production error, an outdated version of the Supporting Information was originally published with this article; in it, Table S2 and Table S3 were exchanged as well as Figures S9 and S10. These errors have been corrected, and this may be considered the authoritative version of record.